

# A Survey of General Relativistic Magnetohydrodynamic Models for Black Hole Accretion Systems

VEDANT DHURV,<sup>1,2</sup> BEN PRATHER,<sup>3</sup> GEORGE WONG,<sup>4,5</sup> AND CHARLES F. GAMMIE<sup>1,2,6</sup>

<sup>1</sup>*Department of Physics, University of Illinois, 1110 West Green St., Urbana, IL 61801, USA*

<sup>2</sup>*Illinois Center for Advanced Study of the Universe, 1110 West Green Street, Urbana, IL 61801, USA*

<sup>3</sup>*CCS-2, Los Alamos National Laboratory, P.O. Box 1663, Los Alamos, NM 87545, USA*

<sup>4</sup>*School of Natural Sciences, Institute for Advanced Study, 1 Einstein Drive, Princeton, NJ 08540, USA*

<sup>5</sup>*Princeton Gravity Initiative, Princeton University, Princeton, New Jersey 08544, USA*

<sup>6</sup>*Department of Astronomy, University of Illinois, 1002 West Green St., Urbana, IL 61801, USA*

## ABSTRACT

General Relativistic Magnetohydrodynamics (GRMHD) simulations are an indispensable tool in studying accretion onto compact objects. The Event Horizon Telescope (EHT) frequently uses libraries of ideal GRMHD simulations to interpret polarimetric, event-horizon-scale observations of supermassive black holes at the centers of galaxies. In this work, we present a library of ten non-radiative, ideal GRMHD simulations that were utilized by the EHT Collaboration in their analysis of Sagittarius A\*. The parameter survey explores both low (SANE) and high (MAD) magnetization states across five black hole spins  $a_* = -15/16, -1/2, 0, +1/2, +15/16$  where each simulation was run out to 30,000 GM/c<sup>3</sup>. We find the angular momentum and energy flux in SANE simulations closely matches the thin-disk value, with minor deviations in prograde models due to fluid forces. This leads to spin equilibrium around  $a_* \sim 0.94$ , consistent with previous studies. We study the flow of conserved quantities in our simulations and find mass, angular momentum, and energy transport in SANE accretion flows to be primarily inward and fluid-dominated. MAD models produce powerful jets with outflow efficiency  $> 1$  for  $a_* = +0.94$ , leading to black hole spin-down in prograde cases. We observe outward directed energy and angular momentum fluxes on the horizon, as expected for the Blandford-Znajek mechanism. MAD accretion flows are sub-Keplerian and exhibit greater variability than their SANE counterpart. They are also hotter than SANE disks within  $r \lesssim 10$  GM/c<sup>2</sup>. This study is accompanied by a public release of simulation data at <http://thz.astro.illinois.edu/>.

## 1. INTRODUCTION

It is now widely believed that supermassive black holes reside at the centers of nearly all galaxies (Lynden-Bell 1969; Kormendy & Richstone 1995; Richstone et al. 1998), are fed by nearby stars and gas clouds, and play a key role in the evolution of the host galaxy (see, e.g., Silk & Rees 1998; Magorrian et al. 1998; King 2003; Hopkins et al. 2024). Of these, Sgr A\* and M87—the putative supermassive black holes at the centers of our Galaxy and M87 galaxy respectively—subtend the largest angle on the sky ( $\sim 50\mu\text{as}$ ). Additionally, near-horizon emission from these sources peaks at millimeter wavelengths, making them suitable for ground-based VLBI observation (Doeleman et al. 2009).

Over the past five years, the EHT—a global array of millimeter wavelength telescopes—has released horizon-scale, total intensity and polarimetric images of M87\* (Event Horizon Telescope Collaboration et al. 2019a,b,c,d,e,f, 2021a,b, 2023, hereafter EHTC M87 I–IX) and Sgr A\* (Event Horizon Telescope Collaboration et al. 2022a,b,c,d,e,f, 2024; The Event Horizon Telescope Collaboration et al. 2024, hereafter EHTC SgrA I–VIII). These images show a bright ring of emission encircling a central depression in brightness, or “shadow”, and are broadly consistent with models of geometrically thick, hot, two-temperature, advection-dominated accretion flows (Ichimaru 1977; Rees et al. 1982; Narayan & Yi 1994, 1995; Narayan et al. 1995).

The theoretical interpretation accompanying these observations is based on a large set of synthetic images and spectral energy distributions (SEDs) generated by carrying out general relativistic radiative transfer (GRRT) calculations on data from GRMHD simulations of supermassive black hole accretion (see Wong et al. 2022).

Summary statistics derived from these electromagnetic observables are compared against observations allowing inferences to be drawn about the source. The observations support magnetically dominated accretion flows and provide constraints on the black hole spin, accretion rate, and the electron-to-ion temperature ratio in the plasma. In the case of Sgr A\*, the analysis also provides constraints on the observer inclination relative to the angular momentum of the accretion flow (EHTC SgrA V).

The EHT theory pipeline relies on a *library* of GRMHD simulations of black hole accretion. The “canonical” set of simulations in these analyses solves the equations of ideal GRMHD for a single-temperature fluid (Gammie et al. 2003; De Villiers & Hawley 2003; Del Zanna et al. 2007; Porth et al. 2019), starting from similar initial conditions across a range of black hole spins and magnetization states (see Section 3.2), using multiple codes (Sądowski et al. 2013; Porth et al. 2017; Prather et al. 2021; Liska et al. 2022). The M87\* and Sgr A\* analysis also considers a selected set of simulations with varying disk geometry (Chatterjee et al. 2020), different initial conditions (Ressler et al. 2020), and additional physics (Ryan et al. 2018; Dexter et al. 2020).

In this paper we present a version of the GRMHD library, which we will refer to as *v3*, generated by the performance-portable, GPU-enabled code KHARMA that was instrumental in analyzing horizon-scale observations of the galactic center (EHTC SgrA V; EHTC SgrA VIII). We limit our analysis to the fluid-level data products, i.e., the spatio-temporal information of the fluid state and the magnetic fields prior to any radiative transfer post-processing. In Section 2 we provide a primer on ideal GRMHD and go over some of the assumptions when modelling low-luminosity active galactic nuclei (LLAGN) using ideal GRMHD. In Section 3 we introduce KHARMA, outline the initial conditions and model parameters for the *v3* library, and discuss the numerical shortcomings of our algorithm. In Section 4, we discuss trends in our GRMHD simulation library by analyzing time-series and time-averaged data. In Section 5 we provide a URL for the GRMHD data used in this paper. We conclude in Section 6 by summarizing our findings and listing the limitations of our model library.

## 2. GENERAL RELATIVISTIC MAGNETOHYDRODYNAMICS (GRMHD)

Since the present work focuses on GRMHD data products, we provide a brief overview of the governing equations, nomenclature of fluid variables, and discuss the assumptions that go into our black hole accretion model.

We adopt a set of units where  $GM = c = 1$ . For the electromagnetic sector we use Lorentz–Heaviside units, which, similar to CGS, set the vacuum permittivity and permeability to unity ( $\epsilon_0 = \mu_0 = 1$ ). However, unlike CGS, Lorentz–Heaviside unit system absorbs factors of  $\sqrt{4\pi}$  into the definition of the electromagnetic fields.

### 2.1. Equations of ideal GRMHD

The governing equations of ideal GRMHD include (i) conservation of particle number, (ii) conservation of energy and momentum (stress-energy tensor) and (iii) the source-free half of Maxwell’s equations. When expressed in a covariant manner these take the form,

$$\begin{aligned}\nabla_\mu(\rho u^\mu) &= 0, \\ \nabla_\mu T^{\mu\nu} &= 0, \\ \nabla_\nu {}^*F^{\mu\nu} &= 0,\end{aligned}\tag{1}$$

where  ${}^*F^{\mu\nu}$  is the dual of the electromagnetic tensor  $F^{\mu\nu}$ ,  ${}^*F^{\mu\nu} = \frac{1}{2}\epsilon^{\mu\nu\alpha\beta}F_{\alpha\beta}$ . Note that Greek indices run over all four dimensions (0, 1, 2, 3) while Latin indices run over the spatial dimensions (1, 2, 3).  $\rho$  is the rest-mass density of the fluid, i.e., it is the density of the fluid as measured by an observer comoving with the fluid (also known as ‘fluid frame’),  $u^\mu$  is the fluid 4-velocity and  $T^{\mu\nu}$  is the ideal MHD stress-energy tensor,

$$T^{\mu\nu} = (\rho + u + p_g + b^2)u^\mu u^\nu + (p_g + \frac{b^2}{2})g^{\mu\nu} - b^\mu b^\nu.\tag{2}$$

$u$  and  $p_g$  are the fluid specific internal energy and pressure respectively, as measured in the fluid frame.  $b^\mu$  is the magnetic-field 4-vector,  $b^\mu \equiv \frac{1}{2}\epsilon^{\mu\nu\kappa\lambda}u_\nu F_{\lambda\kappa}$ . In the fluid frame this has the more intuitive form  $b^\mu \rightarrow (0, \mathbf{B})$ , where  $\mathbf{B}$  is the magnetic field 3-vector measured in the “lab frame”. This relates to the magnetic field measured by the normal observer<sup>1</sup> ( $\mathcal{B}$ ) as  $B^i = \mathcal{B}^i/\alpha = {}^*F^{it}$ . In an arbitrary frame the components of  $b^\mu$  are related to  $\mathbf{B}$  by,

$$\begin{aligned}b^t &= g_{i\mu}B^i u^\mu, \\ b^i &= (B^i + b^t u^i)/u^t.\end{aligned}\tag{3}$$

See Appendix B in Chael et al. (2023) for a more in-depth discussion on degenerate electromagnetic fields in ideal GRMHD. In the ideal MHD limit, electric fields vanish in the fluid frame. Consequently, it can be shown that the 4-vectors  $u^\mu$  and  $b^\mu$  satisfy  $b^\mu u_\mu = 0$ .

<sup>1</sup>The 4-velocity of the normal observer is given by  $\eta_\mu = (-\alpha, 0, 0, 0)$  where  $\alpha \equiv 1/\sqrt{-g_{tt}}$  is the lapse.

We rewrite the equations of ideal GRMHD (Equation 1) in conservation form,

$$\begin{aligned}\partial_t(\sqrt{-g}\rho u^t) &= -\partial_i(\sqrt{-g}\rho u^i) \\ \partial_t(\sqrt{-g}T_\nu^t) &= -\partial_i(\sqrt{-g}T_\nu^i) + \sqrt{-g}T_\lambda^\kappa \Gamma_{\nu\kappa}^\lambda \\ \partial_t(\sqrt{-g}B^i) &= -\partial_j(\sqrt{-g}(b^j u^i - b^i u^j)),\end{aligned}\quad (4)$$

and,

$$\partial_i(\sqrt{-g}B^i) = 0, \quad (5)$$

where we have expressed the equations in a coordinate basis  $x^\mu$ . Equation (5) is the divergence-free criterion for the magnetic fields. Here  $g \equiv \det(g_{\mu\nu})$  is the determinant of the covariant metric and  $\Gamma_{\mu\nu}^\lambda$  is the Christoffel symbol. We assume a  $\hat{\gamma}$ -law equation of state (hereafter EoS),  $p_g = (\hat{\gamma} - 1)u$ , where  $\hat{\gamma}$  is the fluid adiabatic index. The other, inhomogeneous, half of Maxwell's equations,

$$\nabla_\nu F^{\mu\nu} = J^\mu, \quad (6)$$

determines the 4-current  $J^\mu$ .

## 2.2. Assumptions and caveats

The Coulomb collisional mean free paths of the ions and electrons in models of RIAFs are much larger than the length scales associated with the accretion disks (Mahadevan & Quataert 1997). This has two significant implications on the nature of the plasma that is of interest to us.

First, low collisionality suggests that the fluid approach may not be sufficient to capture the relevant physics and a kinetic approach may be in order. However, performing global 3D kinetic simulations is prohibitively expensive, and moreover, Particle-In-Cell (PIC) simulations have shown that microscale instabilities give rise to wave-particle interactions which in turn provide an *effective* collision rate (Kunz et al. 2014; Sironi & Narayan 2015; Sironi 2015; Kunz et al. 2016; Riquelme et al. 2016, 2018; Inchingolo et al. 2018; Bacchini et al. 2022, 2024). This suggests that nonideal effects such as thermal conduction and viscosity may play an important role in the dynamics and thermodynamics of the accreting plasma. Chandra et al. (2015); Foucart et al. (2017) construct one such gyrokinetic model, where the dissipative processes are anisotropic with respect to the local magnetic field. They find the non-ideal effects to not appreciably change the dynamics of the flow for the closure parameters that were considered.

Second, the large thermalization times between the ions and electrons, differences in the heating mechanisms for the two species, and efficient radiative cooling for electrons, implies a two-temperature plasma with the ions being hotter than the electrons (Eardley et al.

1975; Shapiro et al. 1976; Rees et al. 1982; Mahadevan & Quataert 1997). Global simulations of radiatively inefficient accretion flow typically simulate a single temperature fluid and assign electron temperatures during post-processing by apportioning the fluid internal energy based on various electron heating mechanisms and some assumption about the electron distribution function (Mościbrodzka et al. 2016; Wong et al. 2022). Ressler et al. (2015) formulated a sub-grid electron heating scheme where the electrons are modelled as a passive fluid that does not backreact onto the gas. A fraction of the numerical dissipation is appropriated based on the local fluid state and magnetic field (Howes 2010; Rowan et al. 2017; Werner et al. 2018; Kawazura et al. 2019; Zhdankin et al. 2021) and is used to heat the electrons. While this electron entropy tracking procedure is implemented in our code, we do not consider it in this study due to compute and storage limitations at the time. However, a select set of such models was considered in EHTC SgrA V to study how a more detailed treatment of the electron thermodynamics might influence 230 GHz lightcurve variability.

In systems of interest to us we expect the advective motion of the magnetic fields to dominate over diffusion, i.e.,  $\text{Re}_m \gg 1$  ( $\text{Re}_m$  is the magnetic Reynolds number) and ignore explicit resistivity. However, resistive effects are necessary if one wishes to explicitly capture magnetic reconnection that drives particles towards a non-thermal distribution and has been suggested as a possible explanation of near-infrared (NIR) and X-ray flares (Ripperda et al. 2020, 2022; Nathanail et al. 2020; Scepi et al. 2022; Galishnikova et al. 2023; El Mellah et al. 2023; Vos et al. 2024).

For systems accreting far below the Eddington rate,  $\dot{m} \equiv \dot{M}/\dot{M}_{\text{Edd}} \ll 1$  ( $\dot{M}_{\text{Edd}} = 2.2 \times 10^{-8}(M/M_\odot)M_\odot \text{ yr}^{-1}$ , where we have chosen nominal efficiency  $\eta = 0.1$ ), radiative cooling timescales are much longer than inflow timescales and radiation feedback can be ignored. For  $\dot{m} \gtrsim 10^{-6}$ , synchrotron emission and Compton scattering become important, and at higher accretion rates  $\dot{m} \sim 10^{-4}$ , Coulomb collisions also come into the picture (Dibi et al. 2012; Ryan et al. 2017). The accretion rate at the galactic center is believed to be much below this (Quataert & Gruzinov 2000; Bower et al. 2003, EHTC SgrA V) and we do not include radiative cooling.

In our models we set  $\hat{\gamma}$  to a constant value across the simulation domain. This is not true in general since  $\hat{\gamma}$  depends on the local conditions of the fluid. We refer interested readers to Mignone et al. (2005); Mignone & McKinney (2007); Choi & Wiita (2010); Mizuno (2013); Sądowski et al. (2017) for discussions about the limita-

tions of the  $\hat{\gamma}$ -law EoS, physically motivated alternate EoSs, and a scheme to self-consistently evolve adiabatic indices of the electrons and ions.

### 3. NUMERICS AND SIMULATIONS

The quasilinear system of equations that describes ideal GRMHD (Equations 4), are hyperbolic and therefore well-posed (Lichnerowicz 1967; Anile & Pennisi 1987; Anile 1990; Komissarov 1999). The `harm` algorithm (Gammie et al. 2003) is a conservative scheme and consequently (i) ensures convergence to a weak solution of the problem in 1D, if the problem is convergent at all (Lax & Wendroff 1960) and (ii) can capture strong shocks (Hou & Lefloch 1994).

#### 3.1. Code details

The simulation suite presented in this work was generated by KHARMA (Kokkos-based High-Accuracy Relativistic Magnetohydrodynamics with Adaptive Mesh Refinement (AMR); Prather 2024)<sup>2</sup>, a C++17 rewrite of `iharm3d` (Prather et al. 2021) that leverages the Kokkos framework (Carter Edwards et al. 2014; Trott et al. 2021, 2022) to run efficiently on CPUs and GPUs. It utilizes the Parthenon framework (Grete et al. 2022) to (i) achieve block-structured static and adaptive mesh refinement, (ii) introduce flexibility and modularity in the code through the use of dynamic task lists and packages, and (iii) leverage its interface for MPI communication and parallel HDF5 I/O operations.

KHARMA uses a second-order predictor-corrector scheme to step forward in time. The magnetohydrodynamic fields are stored at zone centers and are reconstructed at zone faces using the WENO5 scheme of Jiang & Shu (1996) to compute face-centered transport fluxes. The divergence-free condition (Equation 5) is maintained to machine precision by employing the flux-interpolated constrained transport (flux-CT) scheme of Tóth (2000)<sup>3</sup>. KHARMA solves the Riemann problem at zone faces using the LLF solver (Rusanov 1962). KHARMA evolves 8 scalar fields for ideal GRMHD; these are the set of conserved variables,

$$\mathbf{U} \equiv \sqrt{-g}(\rho u^t, T_t^t, T_i^t, B^i). \quad (7)$$

Additionally, it keeps the corresponding primitive fields,

$$\mathbf{P} \equiv (\rho, u, \tilde{u}^i, B^i), \quad (8)$$

<sup>2</sup> The code is open-source and available at <https://github.com/AFD-Illinois/kharma>

<sup>3</sup> Since the `v3` library was generated, KHARMA now supports the face-centered constrained transport scheme described in Stone & Gardiner (2009).

in lockstep.  $\tilde{u}^i$  is the fluid velocity as measured by the normal observer scaled by the Lorentz factor.<sup>4</sup>

#### 3.2. Initial conditions

We initialize the fluid sector of the simulations with a Fishbone-Moncrief (FM) torus (Fishbone & Moncrief 1976) that is parameterized with the inner radius of the disk,  $r_{\text{in}}$ , and the radius at maximum pressure,  $r_{\text{max}}$ . The thermal energy of the fluid is perturbed to seed development of instabilities such as the MRI (Balbus & Hawley 1991). A detailed description of the implementation of the FM torus can be found in Appendix A of Wong et al. (2022).

The electromagnetic sector of the simulations is initialized with a single poloidal loop of magnetic field by specifying the toroidal component of the magnetic four-vector potential  $A_\phi$ . The strength and structure of the initial field dictates the magnetic flux  $\Phi_{\text{BH}}$  (also expressed in terms of the dimensionless magnetic flux  $\phi_b \sim \Phi_{\text{BH}}/\sqrt{M}$ ) threading the event horizon at steady state and gives rise to two qualitatively different modes of accretion. When  $\phi_b \sim \phi_{b,\text{crit}}$  (where  $\phi_{b,\text{crit}} \sim 15$  is the critical value at which the outward magnetic pressure balances the inward fluid pressure<sup>5</sup>; Tchekhovskoy et al. 2011) we obtain a magnetically arrested disk (MAD) (Bisnovatyi-Kogan & Ruzmaikin 1974, 1976; Narayan et al. 2003; Igumenshchev et al. 2003); the initial magnetic 4-vector potential for which is,

$$A_\phi = \max \left[ \frac{\rho}{\rho_{\text{max}}} \left( \frac{r}{r_{\text{in}}} \sin \theta \right)^3 e^{-r/400} - 0.2, 0 \right], \quad (9)$$

where  $\rho_{\text{max}}$  is the maximum plasma density in the FM torus. When  $\phi_b \ll \phi_{b,\text{crit}}$ , we attain a standard and normal evolution (SANE) disk (Narayan et al. 2012; Sądowski et al. 2013).  $A_\phi(r, \theta)$  for SANE disks in our simulations is given by,

$$A_\phi = \max \left[ \frac{\rho}{\rho_{\text{max}}} - 0.2, 0 \right]. \quad (10)$$

A poloidal slice of the initial conditions for one of our simulations (SANE  $a_* = +0.94$ ) is shown in Figure 1.

<sup>4</sup> In numerical relativity terminology, the fluid velocity relative to a normal (Eulerian) observer with velocity  $n^\mu = \frac{1}{\alpha}(1, -\beta^i)$  is given by  $u^i = \frac{u^i}{\Gamma} + \frac{\beta^i}{\alpha}$ , where  $\beta^i \equiv g^{ti}\alpha^2$  is the shift. Note that  $\Gamma$  is the Lorentz factor of the fluid with respect to the normal observer,  $\Gamma = -n_\mu u^\mu$ . In `harm` we instead consider  $\tilde{u}^i \equiv \Gamma u^i$  for numerical stability reasons.

<sup>5</sup> The value of  $\phi_{b,\text{crit}}$ , a measure of the maximum allowable magnetic flux trapped at the horizon, is believed to depend on the black hole spin and the adiabatic index of the accreting fluid.

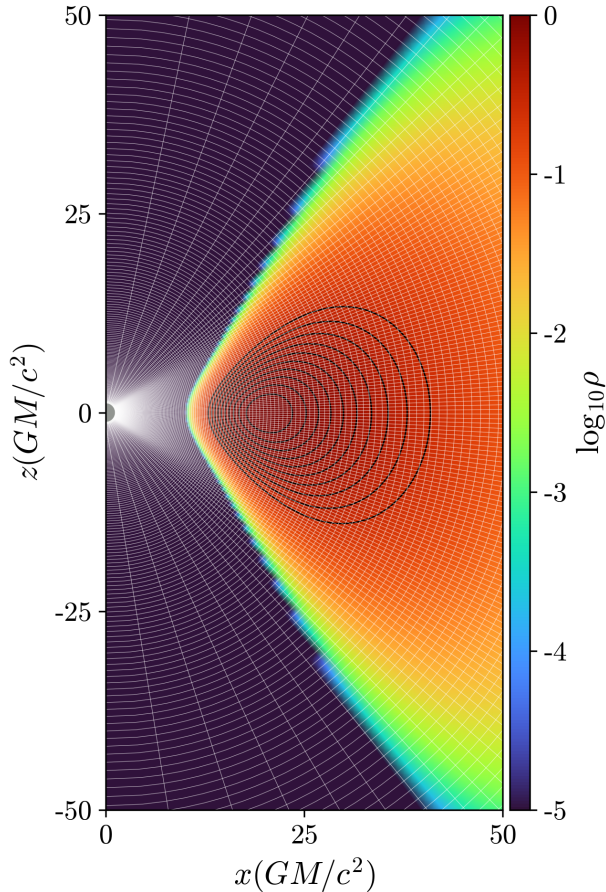


**Figure 1.** Azimuthal/poloidal slice of initial conditions along with the grid geometry. The color scale denotes the logarithm of the rest-mass density and as an example we plot the magnetic fields structure (in black) for a SANE disk. The grid zone boundaries are represented by the white mesh. The grid zones are concentrated towards the equatorial plane and at smaller radii, where we expect most of the relevant physics to occur.

### 3.3. Grid geometry

We integrate the governing equations (Equations 4) in Kerr spacetime with a modified version of the Kerr-Schild (KS) coordinate system dubbed funky modified Kerr-Schild (FMKS) coordinate system  $x^\mu = (x^0, x^1, x^2, x^3)$ . The modification is two-fold:

- We use an exponential radial coordinate  $x^1$  such that  $r = \exp(x^1)$ , which increases the density of grid zones close to the event horizon.
- The polar coordinate is modified to increase the density of grid zones close to the midplane ( $\theta = \pi/2$ ) and to widen the grid zones close to the poles at small radii. The former is done to capture accretion disk physics with higher effective resolu-

tion while the latter increases the timestep in our simulations.

Figure 1 plots the gridlines for one of the simulations considered in this work. For the exact coordinate transformations see Appendix F in Wong et al. (2022) (also see section 4.2.1 in Prather 2022).

### 3.4. Failure modes

GRMHD codes are not robust in regions where the magnetic energy density exceeds the fluid energy density. Truncation errors in the evolution of the conserved quantities  $\mathbf{U}$  can produce unphysical values of fluid quantities  $\mathbf{P}$ . In such scenarios GRMHD codes typically impose “floors” on  $\rho$  and  $u$  to ensure non-negative values, and limit the fluid Lorentz factor  $\Gamma$  to avoid superluminal velocities. For the suite of simulations presented in this work, we apply the floors in the normal observer frame (McKinney et al. 2012) which in turn necessitates an additional  $\mathbf{U} \rightarrow \mathbf{P}$  operation for the floored grid zones<sup>6</sup>. In the event this inversion operation is unsuccessful, we average over neighboring zones that did manage to invert successfully (an operation hereafter referred to as a “fixup”). The details of the application and values of floors and fixups in the library presented in this work are discussed in Appendix B.

### 3.5. Simulation suite

The v3 library consists of 10 GRMHD simulations run out to  $30,000 t_g$  ( $t_g \equiv GM/c^3$  is the light-crossing time) that span the  $(\phi_b, a_*)$  parameter space (hereafter, referred to as the v3 library), where  $a_* \equiv Jc/GM^2$  is the dimensionless black hole spin. Along the  $\phi_b$  axis, we have the MAD and SANE accretion states and along the  $a_*$  axis we consider 5 data points:  $0, \pm 1/2, \pm 15/16$ . To ensure consistency with other GRMHD simulations used in EHTC SgrA V we set  $\hat{\gamma} = 4/3$ . We list the model parameters for the simulation library in Table 1.

### 3.6. Resolving the MRI

The MRI facilitates the outward transport of angular momentum in a differentially rotating accretion disk with a weak magnetic field. The linear instability amplifies the seed magnetic field and causes a breakdown of the laminar flow into turbulence. The turbulent shear stress that arises acts as the primary channel for radial

<sup>6</sup> We use the “1D<sub>W</sub>” scheme (Noble et al. 2006) as outlined in Mignone & McKinney (2007). This involves a 1D Newton-Raphson solve for the fluid primitives. The magnetic field primitives can be recovered analytically as they differ from the conserved variables by a multiplicative factor of  $\sqrt{-g}$ .

**Table 1.** GRMHD Simulation Suite

Flux	$a_*$	$r_{\text{in}} (r_g)$	$r_{\text{max}} (r_g)$	$r_{\text{out}} (r_g)$	$\hat{\gamma}$	Resolution	Duration ( $t_g$ )
MAD	-0.94	20	41	1000	4/3	288x128x128	30,000
MAD	-0.5	20	41	1000	4/3	288x128x128	30,000
MAD	0	20	41	1000	4/3	288x128x128	30,000
MAD	0.5	20	41	1000	4/3	288x128x128	30,000
MAD	+0.94	20	41	1000	4/3	288x128x128	30,000
SANE	-0.94	10	20	1000	4/3	288x128x128	30,000
SANE	-0.5	10	20	1000	4/3	288x128x128	30,000
SANE	0	10	20	1000	4/3	288x128x128	30,000
SANE	0.5	10	20	1000	4/3	288x128x128	30,000
SANE	+0.94	10	20	1000	4/3	288x128x128	30,000

NOTE—Simulation parameters: Flux specifies the amount of magnetic flux threading the event horizon and can be MAD or SANE (see section 3.2),  $a_*$  is the dimensionless black hole spin,  $\hat{\gamma}$  is the fluid adiabatic index,  $r_{\text{in}}$  and  $r_{\text{max}}$  are the inner and pressure maximum radii of the FM torus, and  $r_{\text{out}}$  is the radial outer boundary of the simulation domain, all in units of  $r_g \equiv GM/c^2$ . Resolution denotes the number of grid zones along each direction like  $N_r \times N_\theta \times N_\phi$ . Duration is the total duration of the simulation in units of  $t_g$ .

transport of angular momentum in the SANE simulations.

We check if we are able to resolve the fastest growing mode of the MRI by computing “MRI quality factors” ( $Q_{\text{MRI}}^\theta$  and  $Q_{\text{MRI}}^\phi$ ; Sano et al. 2004; Noble et al. 2010; Hawley et al. 2011, 2013; Narayan et al. 2012; Porth et al. 2019). These indicate the number of zones capturing the wavelength of the particular mode of the MRI along the polar and azimuthal direction respectively. In the SANE simulations we find  $Q_{\text{MRI}}^\theta \sim 5 - 10$  and  $Q_{\text{MRI}}^\phi \sim 12 - 16$ <sup>7</sup>. While this is below the nominal values of  $Q_{\text{MRI}}^{\theta,\phi} \sim 10, 20$  suggested by Hawley et al. (2011); Narayan et al. (2012), we do achieve the minimum bound of  $Q_{\text{MRI}}^\theta \geq 6$  prescribed by Sano et al. (2004) in most of our simulations.

## 4. DIAGNOSTICS AND RESULTS

### 4.1. Radial fluxes at the horizon

In this subsection we study trends in the at-horizon radial fluxes in our simulation set.

#### 4.1.1. Time series

We evaluate radial fluxes of the rest-mass, magnetic field, total angular momentum and energy at the event

<sup>7</sup> These are time- and azimuth-averaged values that were computed in the midplane of our simulation domain, from the inner radial boundary out to  $r = 50r_g$ .

horizon ( $r_{\text{eh}} \equiv 1 + \sqrt{1 - a_*^2}$ )<sup>8</sup>,

$$\dot{M} = \int_\phi \int_\theta (-\rho u^r) \sqrt{-g} d\theta d\phi, \quad (11)$$

$$\Phi_{\text{BH}} = \frac{1}{2} \int_\phi \int_\theta |B^r| \sqrt{-g} d\theta d\phi, \quad (12)$$

$$\dot{L} = \int_\phi \int_\theta T_\phi^r \sqrt{-g} d\theta d\phi, \quad (13)$$

$$\dot{E} = \int_\phi \int_\theta (-T_t^r) \sqrt{-g} d\theta d\phi, \quad (14)$$

where the integrals over  $(\theta, \phi)$  are over the entire shell.<sup>9</sup>  $\dot{M}$  is the *inward* rate of matter. Equation 12 counts the *total* number of magnetic field lines threading the horizon, irrespective of the direction, and then halves to account for just one hemisphere. In Appendix A we discuss the caveats associated this definition. The components of  $T_\nu^\mu$  corresponding to angular momentum and energy are obtained by contracting it with the respective Killing vector fields,  $\xi_{(t)}^\mu \equiv \partial_t$  and  $\xi_{(\phi)}^\mu \equiv \partial_\phi$  (see Section 4.4). Note that  $\dot{L}$  and  $\dot{E}$  here describe the *outflow* of angular momentum and energy.

Ideal GRMHD has no inherent length, time, or density scale and quantities can be scaled in accordance with the physical system being analyzed during post-processing.

<sup>8</sup> In MAD models we measure  $\dot{M}$ ,  $\dot{L}$  and  $\dot{E}$  at  $r = 5 r_g$ . This is done to avoid the effect of density floors that tend to produce a noticeable difference in the MAD simulations (see relative difference in  $\dot{M}$  in Table 2)

<sup>9</sup> The equations here are expressed in Kerr-Schild coordinates for clarity, but we perform the integration in FMKS coordinates.

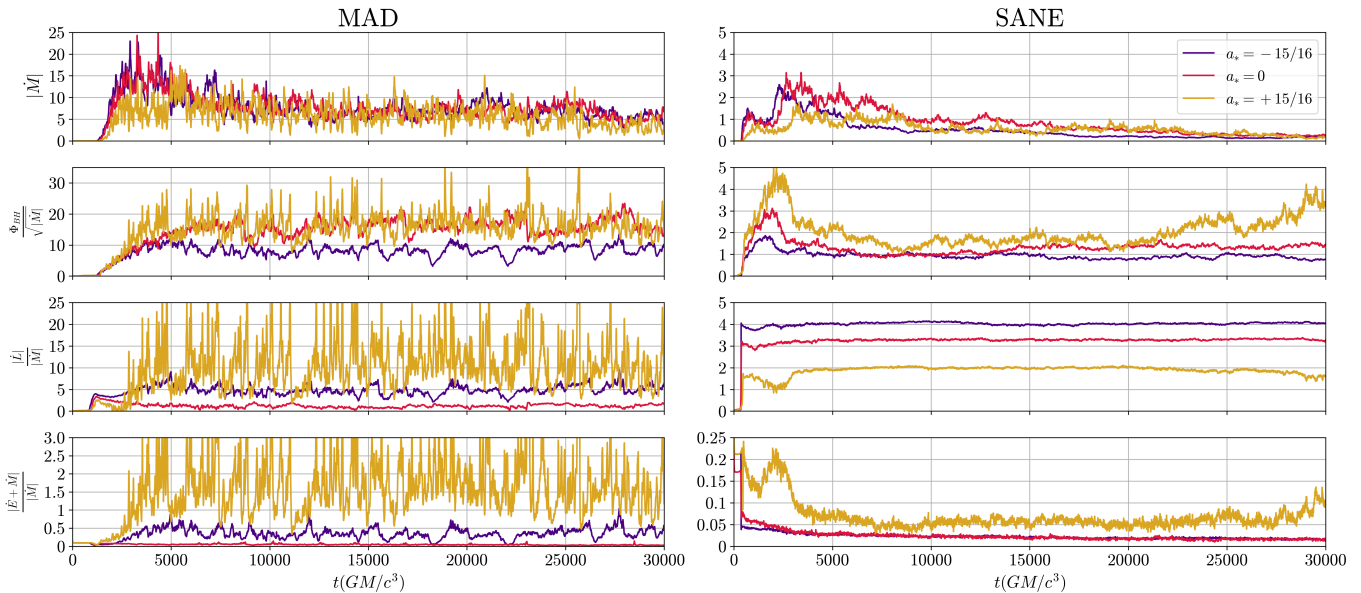


**Figure 2.** Time series of the horizon-penetrating fluxes for six models:  $a_* = \{-15/16, 0, +15/16\}$ , MAD and SANE. Left column: MAD simulations. Right column: SANE simulations. Top row: Rest-mass accretion rate. Second row: Dimensionless magnetic flux. Third row: Normalized, absolute angular momentum flux. Bottom row: Normalized absolute energy flux with the contribution from rest mass subtracted.  $a_* = -15/16$  simulations are plotted in indigo,  $a_* = 0$  simulations in crimson, and  $a_* = +15/16$  in goldenrod.

As a result we normalize the fluxes by appropriate powers of the accretion rate.

We plot the time series of these quantities for six of our models in Figure 2. We see in the accretion rate plot (top panels) that following the initial rise in  $\dot{M}$  as matter first crosses the event horizon, there is a decline, and ultimately  $\dot{M}$  saturates to a quasi-steady value. The time at which this steady state is achieved varies from model-to-model, but by 15,000  $t_g$  all models have attained this state. In the remainder of this paper we consider data in the range  $t = [15, 30] \times 10^3 t_g$  when computing time-average of quantities.

The SANE models tend to have a steady flow with smaller variations in all the radial fluxes. They are characterized by an almost uniform inflow of material across the horizon with the magnetic field playing a negligible role in the flow dynamics other than to transfer angular momentum outward. In MAD models the magnetic flux at the horizon saturates to its maximum value  $\phi_{b,crit}$  soon after accretion commences. At this stage, the flow near the horizon is in a state of unstable equilibrium as the outward magnetic pressure counterpoises the inward fluid pressure. This is colloquially known as an “arrested” state. This is followed by a release of excess magnetic flux (dubbed as a “flux eruption” event) and  $\phi_b$  drops while  $\dot{M}$  rises. These intermittent flux eruption events result in the larger fluctuations in the time series for the MAD models.

#### 4.1.2. Time-averaged

We plot the time-averaged, normalized angular momentum ( $l \equiv \dot{L}_{in}/\dot{M}$ ) and energy ( $e \equiv \dot{E}_{in}/\dot{M}$ ) fluxes in the left and middle panels respectively in Figure 3. It is worth noting that (i) these are the *inflowing* radial fluxes at the horizon, i.e., they differ by a negative sign from Equations 13, 14, and (ii) these are signed quantities unlike Figure 2 where we showed the absolute values of the fluxes. The right panel in Figure 3 plots the “efficiency” of the system. This is the ratio of mechanical power flowing out to the power flowing in due to fluid rest-mass accreting. Thin disk values at the innermost stable circular orbit  $r_{isco}$  (Shakura & Sunyaev 1973; Bardeen et al. 1972) are denoted by dashed lines. This corresponds to inflow of cold, unmagnetized gas in the equatorial plane.

The time-averaged specific angular momentum flux in SANE models closely follows the thin disk expectation.  $l > 0$  for all spins indicates a net inflow of angular momentum into the black hole. The  $a_* \leq 0$  MAD models also exhibit a net transfer of angular momentum into the black hole from the surroundings. However, the prograde MAD models possess a powerful jet, with highly collimated magnetic field lines anchored at the horizon. These field lines remove angular momentum from the black hole and result in a net outflow (see Section 4.6).

In the SANE simulations, most of the energy is advected into the black hole, and the deviation from the

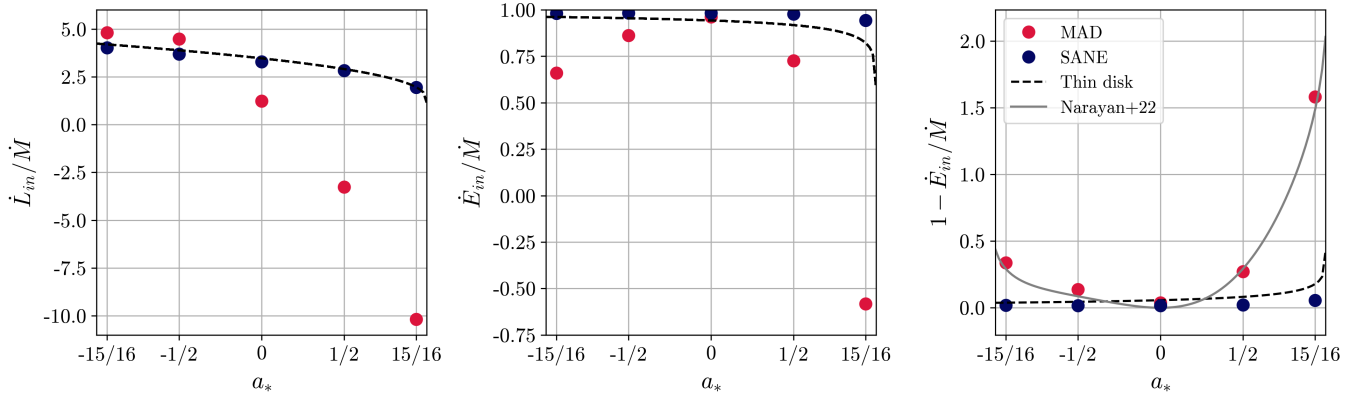


**Figure 3.** Time-averaged radial fluxes as a function of black hole spin. The data points in red (blue) denote MAD (SANE) simulations. The dashed line plots the value expected for a thin disk at the ISCO. Left panel: Specific angular momentum flux. Middle panel: Specific energy flux. Right panel: Ratio of outflow power ( $\dot{E} - \dot{M}$ ) to rest-mass accretion rate.

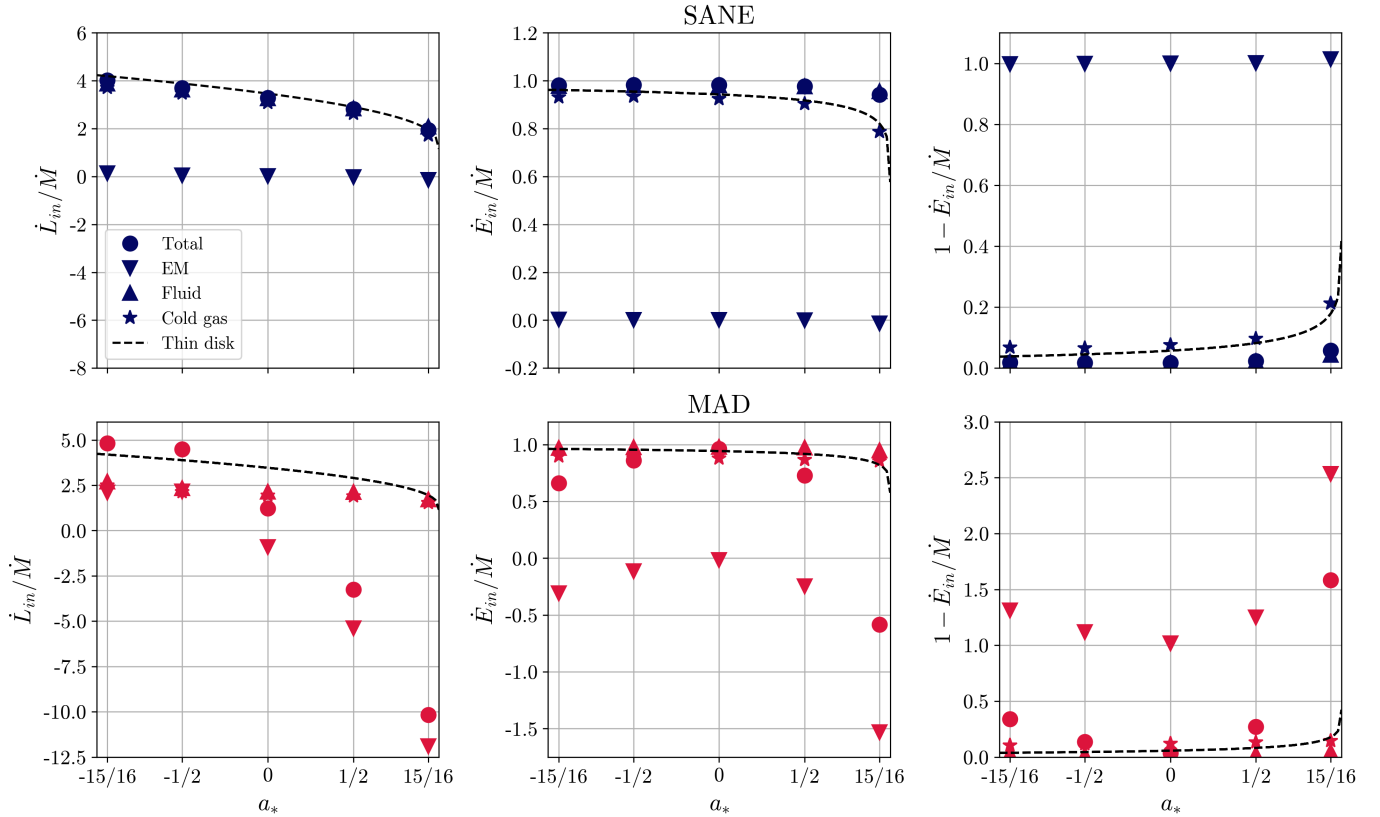


**Figure 4.** Similar to Figure 3 but now plotting the contribution of various components of the fluxes (See Equations 15,16, 17, 18, 19, and 20). We see that magnetic fields have little-to-no contribution toward  $\dot{L}$  and  $\dot{E}$  in SANE models. In the MAD models the trend in total flux closely matches the trend observed in the electromagnetic components.



thin disk estimate grows as  $a_*$  increases. We explore this in detail in the following paragraphs where we break down the contributions to these fluxes (Figure 4). MAD models generally exhibit substantially higher efficiencies with prograde models being more efficient than their retrograde counterparts. This aligns with results of Tchekhovskoy & McKinney (2012); Tchekhovskoy et al. (2012); Narayan et al. (2022).

Figure 4 deconstructs the radial fluxes plotted in Figure 3 into its electromagnetic,

$$l^{(\text{EM})} = \frac{\langle -b^2 u^r u_\phi + b^r b_\phi \rangle_t}{\langle -\rho u^r \rangle_t}, \quad (15)$$

$$e^{(\text{EM})} = \frac{\langle b^2 u^r u_t - b^r b_t \rangle_t}{\langle -\rho u^r \rangle_t}, \quad (16)$$

and fluid,

$$l^{(\text{fl})} = \frac{\langle -(\rho + u + p_g) u^r u_\phi \rangle_t}{\langle -\rho u^r \rangle_t}, \quad (17)$$

$$e^{(\text{fl})} = \frac{\langle (\rho + u + p_g) u^r u_t \rangle_t}{\langle -\rho u^r \rangle_t}, \quad (18)$$

components.  $\langle \rangle_t$  denotes a time-averaging. Additionally, we plot the fraction of the fluid component corresponding to a cold gas,

$$l^{(\text{cg})} = \frac{\langle -\rho u^r u_\phi \rangle_t}{\langle -\rho u^r \rangle_t}, \quad (19)$$

$$e^{(\text{cg})} = \frac{\langle \rho u^r u_t \rangle_t}{\langle -\rho u^r \rangle_t}. \quad (20)$$

As one might expect, the electromagnetic components of the normalized fluxes are approximately zero in the SANE models due to the subdominant role of the magnetic fields. For the specific angular momentum flux, the cold gas component nearly accounts for the entire fluid contribution. In the case of specific energy flux, the cold gas component closely resembles that of a thin disk. Additionally, we observe that as spin increases, the thermodynamic contribution of the fluid becomes more significant, consistent with Figure 9, which shows an increase in fluid temperature with higher  $a_*$ . In MAD simulations, the electromagnetic component dominates the diagnostic trends, except in the non-spinning case. The specific energy flux in the fluid sector is approximately evenly distributed between rest-mass energy and internal energy.

#### 4.1.3. Time variability of $\dot{M}$

The primary motivation for this library was to provide a physical interpretation of the 2017 EHT observation of the galactic center (EHTC SgrA V) in conjunction with historical multifrequency observations of Sgr A\*. In total, 11 heterogeneous constraints were applied to infer

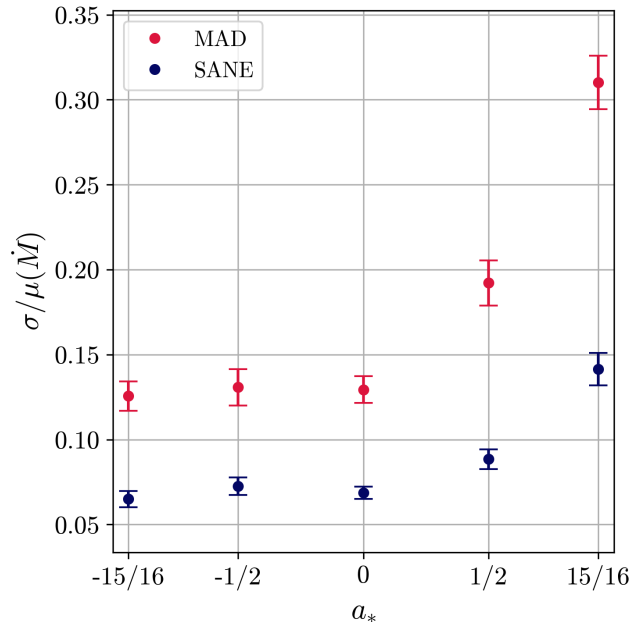


**Figure 5.** 3hr modulation index  $M_3$  for the accretion rate  $\dot{M}$  (defined as  $M_{\Delta t} \equiv \sigma_{\Delta t}/\mu_{\Delta t}$ ; here  $\Delta t = 3\text{hr}$ ). To estimate the average  $M_3$  (indicated by a marker for each simulation in this plot) for SgrA\* (which has a characteristic timescale  $t_g \sim 20$  s), we extract as many independent 3 hour time segments from the  $\dot{M}$  time series from  $t=15,000t_g$  to  $t=30,000t_g$  ( $\sim 27$ ) and compute the average sample mean. The errorbars plot the standard error of the sample means ( $\sim \sigma_{M_3}/\sqrt{27}$ ) and quantify the uncertainty in our measurement of  $M_3$ .

properties of the source. To minimize the possibility of wrongly rejecting a model, the GRMHD simulations were run out for a longer duration compared to previous work (Wong et al. 2022) to generate a larger set of independent samples of synthetic observations. This is particularly important when assessing model feasibility based on the 230GHz light curve variability (see the discussion in EHTC SgrA V and Wielgus et al. 2022).

In this subsection we study the time variability in  $\dot{M}$ . While this does not directly translate to variability in the image-integrated flux density<sup>10</sup>, it can be a reasonable proxy given that most of the 230GHz compact flux observed by the EHT arises close to the event horizon (see, e.g., Porth et al. 2019 or Figure 5 in Wong et al. 2022).

In Figure 5 we present the time variability in  $\dot{M}$  for Sgr A\*. The average and standard error of the sam-

<sup>10</sup> The synchrotron emissivity for a population of relativistic thermal electrons is a function of the electron number density, magnetic field strength, electron temperature, and frequency (Leung et al. 2011). Additionally, geometric effects such as gravitational lensing and Doppler beaming can alter the horizon-scale image and, in-turn, change the observed flux density.

ple means of the modulation index (defined as  $M_{\Delta t} \equiv \sigma_{\Delta t}/\mu_{\Delta t}$  for a time duration  $\Delta t$ ) are computed in a manner similar to the variability analysis in EHTC SgrA V. Independent 3 hour segments, corresponding to the typical decorrelation timescale in our GRMHD simulations (see Wielgus et al. 2022), are extracted from the  $\dot{M}$  time series starting at  $t=15,000t_g$ , and we calculate the sample mean  $M_3$  ( $\Delta t = 3$  hours,  $\sim 530 t_g$  for Sgr A\*). The errorbars reflect our uncertainty in measuring the average  $M_3$ , which is directly proportional to the standard deviation of each sample, and inversely proportional to the number of independent samples. Two clear trends emerge: (i) MAD models exhibit significantly more variability than their SANE counterparts with the same black hole spin, a finding also reflected in the light curve variability, and (ii)  $M_3$  is higher for models with  $a_* > 0$ , while retrograde models with the same magnetization state (MAD or SANE) show comparable  $M_3$  values.

#### 4.2. Inflow equilibrium

We initialize our simulations with a Fishbone-Moncrief torus, a solution to the relativistic Euler equations in a stationary spacetime, and perturb the internal energy to seed instabilities, such as the MRI, which drive accretion (see Section 3.2). The evolution of the accretion disk can be sensitive to the initial conditions. To reduce their influence on the GRMHD (or GRRT) data products, simulations must be run out for longer periods, allowing the system to reach a steady state “inflow equilibrium” at larger radii. In this section we assess the radial extent over which our simulations achieve inflow equilibrium using two diagnostics.

First, we examine the time-averaged accretion rate as a function of radius  $\dot{M}(r)$ . As the fluid orbits the black hole, the velocity gradient induces a shear force between neighboring fluid annuli, generating viscous torques that transfer angular momentum outward and drive inflow (see, e.g., Lynden-Bell 1969; Shakura & Sunyaev 1973; Novikov & Thorne 1973; Page & Thorne 1974; Lynden-Bell & Pringle 1974; Pringle 1981; Frank et al. 1985; Papaloizou & Lin 1995). In steady-state accretion disk theory,  $\dot{M}$  is constant and independent of radius. In our simulations, however, we do not expect  $\dot{M}$  to remain constant over time due to the finite reservoir of material, which depletes through both accretion into the black hole and outflows<sup>11</sup>. Nevertheless, as the simulation progresses, we expect the  $\dot{M}$  profile to attain a constant value. To estimate an inflow equilibrium radius  $r_{\text{eq}}$  from  $\dot{M}(r)$  profiles, we adopt the criterion from White et al.

**Table 2.** Inflow equilibrium and accretion rate statistics

Flux	$a_*$	$\dot{M}$ difference (%)	$r_{\text{eq}}(\dot{M})$	$r_{\text{eq}}(t_{\text{in}})$
MAD	-15/16	6.09	64.00	50.65
MAD	-1/2	7.35	65.55	51.32
MAD	0	8.56	70.59	49.65
MAD	+1/2	12.15	59.97	46.96
MAD	+15/16	20.40	45.06	45.06
SANE	-15/16	0.13	30.99	26.31
SANE	-1/2	0.17	30.09	26.33
SANE	0	0.39	31.98	27.41
SANE	+1/2	0.89	28.15	22.54
SANE	+15/16	1.77	18.52	17.67

NOTE—The first two columns are identical to Table 1. The third column mentions the relative difference in  $\dot{M}$  when measured at  $r_{\text{ch}}$  vs  $5r_g$ ,  $r_{\text{eq}}(\dot{M})$  and  $r_{\text{eq}}(t_{\text{in}})$  are the radial extent to which the flow has achieved steady state as measured from  $\dot{M}(r)$  and  $t_{\text{in}}(r)$  respectively.

(2020), where the inflow equilibrium radius is defined as the radius at which  $\dot{M}$  drops to  $e^{-1/2}$  of its value at the horizon ( $5 r_g$  in the case of MAD simulations). The  $r_{\text{eq}}$  values for our simulations are listed in Table 2.

Second, we evaluate the inflow timescale,

$$t_{\text{in}}(r) \equiv \frac{r}{\langle -v^r \rangle}, \quad (21)$$

where  $v^r$  is the radial component of the spatial fluid velocity measured by the normal observer,  $v^i = u^i/u^t$ . This is often referred to as the viscous timescale (Penna et al. 2010; Narayan et al. 2012) as it represents the time required for viscous diffusion at a given radius  $r$ . Figure 6 shows the time-averaged  $t_{\text{in}}$  as a function of radius. As expected, the inflow time increases with radius. The MAD simulations exhibit lower  $t_{\text{in}}$  at the same radii compared to SANE simulations, indicating a higher inward radial velocity, consistent with findings of Narayan et al. (2012). Notably, in SANE simulations,  $t_{\text{in}}$  increases with increasing  $a_*$ . The dashed lines represent powerlaws  $\sim r^{5/2}$  that approximate  $t_{\text{in}}(r)$ , which is steeper than the thin-disk expectation  $t_{\text{in}} \sim r/v^r \sim r^2/\nu \sim r/(\alpha c_s(H/r)) \sim r^{3/2}/(\alpha(H/r)^2)$ , assuming a constant  $\alpha$ .  $c_s$  is the local sound speed, and  $\nu$  is the coefficient of kinematic viscosity. We define  $r_{\text{eq}}$  as the radius where the inflow timescale matches the simulation run time<sup>12</sup>. The final column in Table 2 lists  $r_{\text{eq}}$  computed using the inflow timescale.

<sup>11</sup> There are also small-scale turbulent fluctuations, but time-averaging is expected to smooth these out.

<sup>12</sup> We consider the end of the simulation when evaluating the simulation run time.

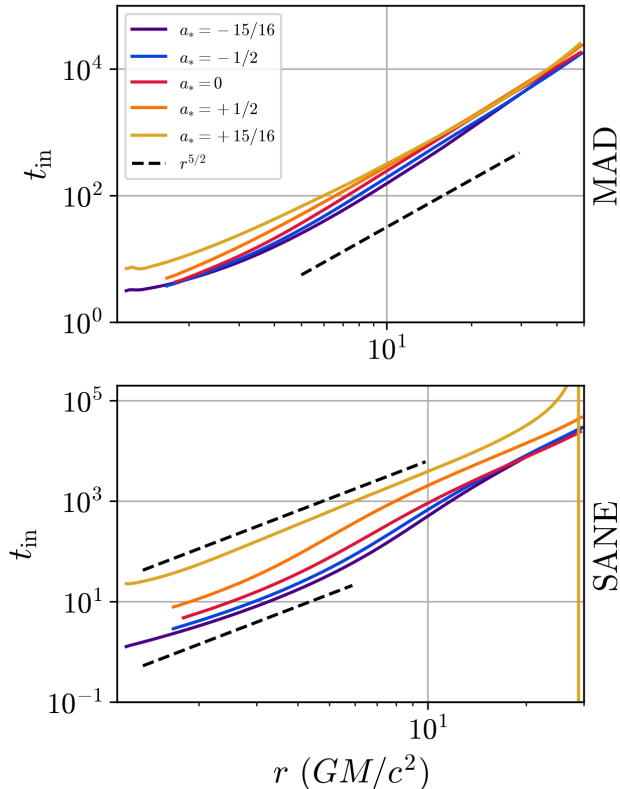


**Figure 6.** Time-averaged, density-weighted radial profiles of  $t_{\text{in}}$  for the `v3` library. The dashed lines are power laws that approximately trace  $t_{\text{in}}$ .

#### 4.3. Time-averaged disk structure

It is instructive to look at the time- and azimuth-averaged quantities to infer broad characteristics of the flow. In Figure 7, we present poloidal slices of the rest-mass density  $\rho$ , plasma magnetization  $\sigma$ , and fluid temperature  $p_g/\rho$ , all averaged in time and azimuth. The contours indicate the  $\sigma = 1$  surface, which we use to delineate the magnetically dominated jet from the disk. MAD accretion disks are hotter than their SANE counterparts, a trend more clearly shown in Figure 9 where we plot disk-averaged radial profiles. The halo of high density close to the black hole in the MAD simulations is due to numerical floors. We discuss this in greater detail in Appendix B.

In Figure 8 we present the jet profiles ( $\sigma = 1$  contours). The MAD models exhibit a wider jet compared to the corresponding SANE models. In the SANE  $a_* = -0.5, 0, +0.5$  simulations, the outflow is too weak to sustain a persistent jet, causing the  $\sigma = 1$  contour to loop back inward. Unlike Narayan et al. (2022), we do not observe a strong dependence of the jet profile on spin in the MAD models, possibly due to the shorter duration of our simulations. We also show powerlaws ap-

proximating the jet profiles near the black hole:  $z \propto r^{1.3}$  for the MAD simulations and  $z \propto r^{1.9}$  for the SANE simulations. These results are consistent with previous numerical studies (McKinney 2006; Narayan et al. 2022) and observational work on AGNs (Asada & Nakamura 2012), which predict a parabolic jet profile within the inner  $\sim 10^4 r_g$ .

Figure 9 shows radial profiles of the rest-mass density  $\rho$ , fluid temperature  $p_g/\rho$ , fluid entropy  $s \equiv (\hat{\gamma} - 1) \log(p_g/\rho^{\hat{\gamma}})$ , the radial component of the fluid velocity  $v^r$ , the specific angular momentum  $u_\phi$ , specific energy  $u_t$ , the magnetic field strength squared  $b^2$ , the ratio of magnetic to gas pressure  $b^2/(2p_g)$ , and the density scale height  $h/r$ . We compute a density-weighted average,

$$\langle q(r) \rangle_{t,\phi} \equiv \frac{\int \int \int q(t, r, \theta, \phi) \cdot \rho(t, r, \theta, \phi) \cdot \sqrt{-g} dt d\theta d\phi}{\int \int \int \rho(t, r, \theta, \phi) \cdot \sqrt{-g} dt d\theta d\phi}, \quad (22)$$

for  $p_g/\rho, s, v^r, u_\phi, u_t, b^2$  and  $b^2/(2p_g)$  to highlight the behavior of these quantities in the accretion disc. The density profile is volume-averaged. For quantities that are ratios of independent variables, e.g.,  $b^2/(2p_g)$ , we compute the density-weighted average of each variable separately before calculating the ratio. The density scale height is computed as,

$$\frac{h}{r}(r) \equiv \frac{\int \int \int \rho(t, r, \theta, \phi) |\pi/2 - \theta| \cdot \sqrt{-g} dt d\theta d\phi}{\int \int \int \rho(t, r, \theta, \phi) \cdot \sqrt{-g} dt d\theta d\phi}. \quad (23)$$

We find the MAD models are approximately an order of magnitude hotter than the SANE simulations within the inner  $\sim 10 r_g$ , likely due to compressional heating. In MAD simulations, the magnetically dominated, wider jets constrain accretion to narrow channels. In the case of SANE simulations the temperature increases with increasing  $a_*$ .

The ratio of magnetic pressure to gas pressure is higher in MAD simulations. For MAD simulations, the radial fluid velocity seems to follow a power law  $\langle v^r \rangle \propto r^{3/2}$ , independent of spin. In contrast,  $\langle v^r \rangle$  decreases with increasing  $a_*$  in the inner  $\sim 10 r_g$  for SANE simulations. This is expected if the fluid begins to plunge within the ISCO due to insufficient centrifugal support. The average specific angular momentum  $\langle u_\phi \rangle$  is a strong function of  $a_*$  in SANE flows, with retrograde models transferring angular momentum to the black hole more efficiently, reaffirming the findings in Section 4.1 and specifically Figure 4. However, in MAD models, the spin dependence is less pronounced. The density scale height  $h/r$  is directly proportional to  $a_*$  for SANE simulations. Notably, for the SANE models (i) the radial structure and (ii) the spin dependence of the average temperature, specific angular momentum, and scale height agree remarkably well with the semi-analytical

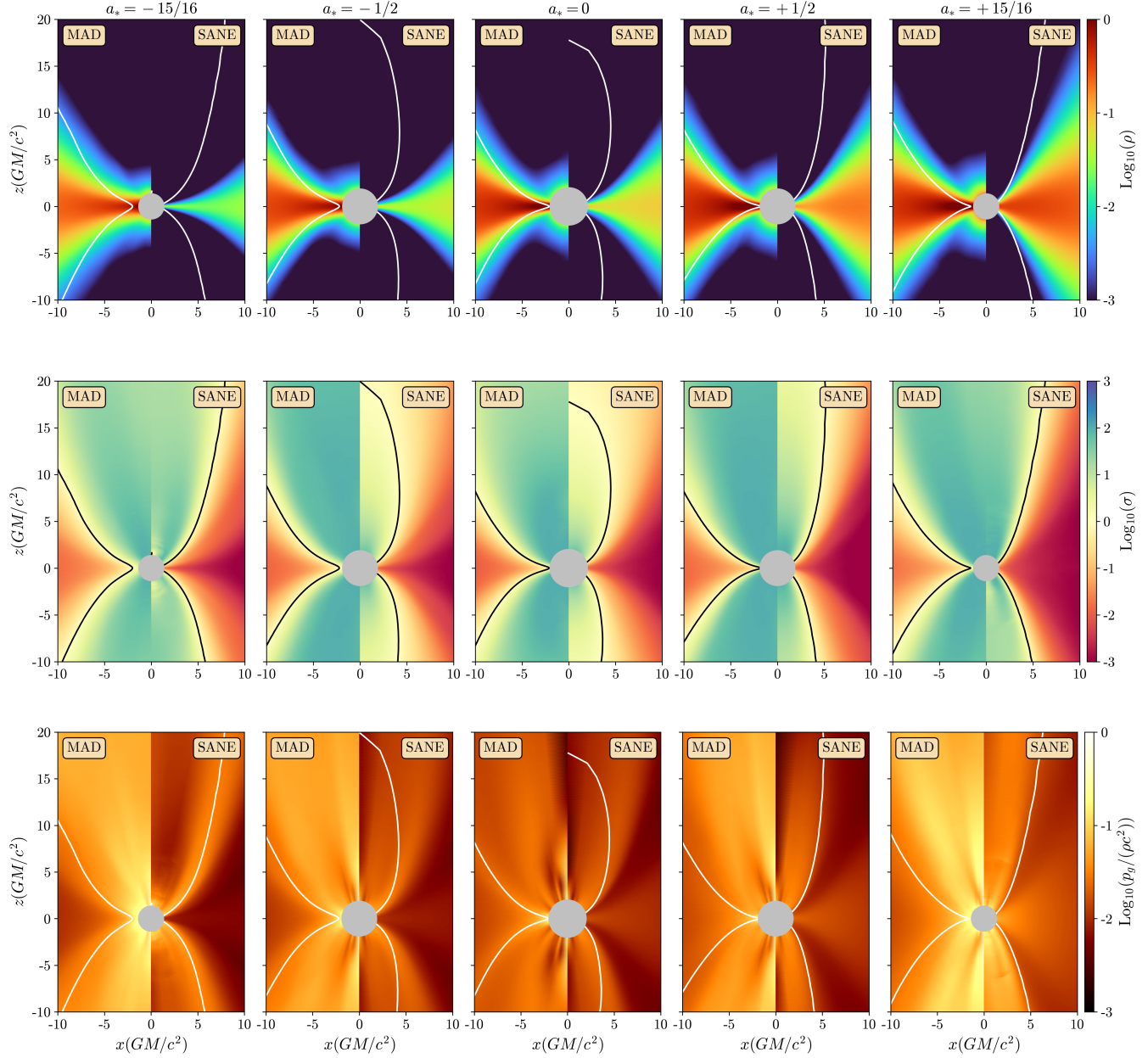


**Figure 7.** Top to bottom: time- and azimuth-averaged poloidal plots of  $\rho$ ,  $\sigma \equiv b^2/\rho$ , and  $\Theta \equiv p_g/(\rho c^2)$  respectively. Each column represents a different black hole spin. In each subplot, the left panel shows the MAD simulation, while the right panel shows the corresponding SANE simulation. Contours in each plot indicate  $\sigma = 1$ . Note that for quantities defined as ratios, such as magnetization  $\sigma$  and fluid temperature  $\Theta$ , the averages are taken separately, e.g.,  $\langle \sigma \rangle = \langle b^2 \rangle / \langle \rho \rangle$ .

model of Gammie & Popham (1998); Popham & Gammie (1998) which solves the height-integrated, axisymmetric equations of relativistic hydrodynamics with a causal prescription for the viscous stress-energy tensor.

In Figure 10 we plot the density-weighted average angular velocity  $\langle \Omega \rangle \equiv \langle u^\phi \rangle / \langle u^t \rangle$ . The MAD simulations exhibit sub-Keplerian behavior with significant variance in azimuthal fluid velocity. SANE flows closely follow

the Keplerian profile and display a more organized angular motion.

#### 4.4. Conserved currents

The motion of ideal fluids in a stationary and axisymmetric metric gives rise to three *conserved currents*. Particle number conservation generates a mass current  $J_M^\mu \equiv \rho u^\mu$  which is conserved along the flow. An equivalent coordinate-dependent current density  $\mathfrak{J}_M \equiv$

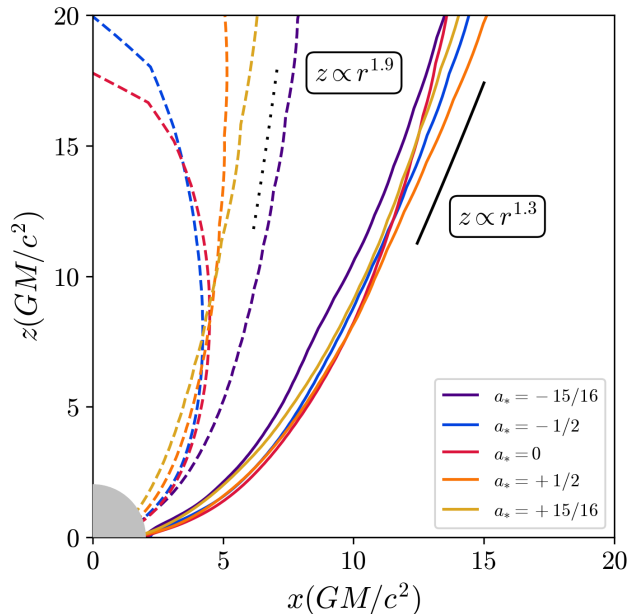


**Figure 8.** Time- and azimuth-averaged “jet profiles” ( $\sigma = 1$  contours). The solid (dashed) lines represent MAD (SANE) models. The filled grey circle at the lower left corner denotes a zero spin black hole ( $r_{\text{eh}} = 2 r_g$ ).

$\sqrt{-g}\mathbf{J}_M$  can also be defined, which will prove beneficial as we plot and compare quantities in a coordinate frame. The Kerr metric is independent of  $t$  and  $\phi$ , i.e., there exist one-parameter family of diffeomorphisms or “isometries” generated by associated Killing vector fields  $\xi_t$  and  $\xi_\phi$  such that the Lie derivative of the metric along these vector fields is zero. In the Kerr-Schild coordinates these vector fields are given by,

$$\xi_t^\mu = \{1, 0, 0, 0\}, \quad \xi_\phi^\mu = \{0, 0, 0, 1\}. \quad (24)$$

The Killing equation  $\nabla_{(\mu}\xi_{\nu)} = 0$  combined with the conservation of the stress-energy tensor gives rise to two additional currents:  $J_E^\mu \equiv -\xi_t^\nu T_\nu^\mu$ , representing the flow of total energy, and  $J_L^\mu \equiv \xi_\phi^\nu T_\nu^\mu$ , representing the flow of angular momentum. The corresponding current densities are  $\mathfrak{J}_E \equiv \sqrt{-g}\mathbf{J}_E$  and  $\mathfrak{J}_L \equiv \sqrt{-g}\mathbf{J}_L$ . Henceforth, we will refer to these current densities simply as currents, as we focus on coordinate-dependent quantities.

In this section we compute conserved currents for the v3 simulation library and examine trends in the flow of mass, angular momentum and energy as a function of black hole spin and magnetization state. The first row in Figure 11 plots the time- and azimuth-averaged conserved currents for the MAD  $a_* = +0.94$  model. Streamlines are overlaid on the average rest-mass density to help interpret the structure of the conserved currents in relation to the overall flow. The colorscale of the streamlines indicates the magnitude of the conserved

currents, spaced logarithmically. Advection-dominated accretion drives strong inflow of mass, angular momentum and energy in the disk. Moving to higher latitudes, the flow lines shift from ingoing to outgoing, with the reversal in the mass current direction indicating the presence of weak MHD winds that produce modest mass outflows. The outflowing streamlines of angular momentum and energy currents, originating from the inner accretion flow region ( $r \lesssim 10 r_g$ ) are highly collimated and anchored at the black hole horizon. Maximal outflow follows a parabolic profile, suggesting the winding of magnetic field lines around the polar axis through the Blandford-Znajek (BZ) mechanism (Blandford & Znajek 1977).

To assess the electromagnetic and fluid contributions to the conserved currents, we perform the following decomposition,

$$J_{L,EM}^\mu = \langle b^2 u^\mu u_\phi - b^\mu b_\phi + \delta_\phi^\mu b^2 / 2 \rangle, \quad (25)$$

$$J_{L,FI}^\mu = \langle (\rho + u + p_g) u^\mu u_\phi + \delta_\phi^\mu p_g \rangle,$$

and,

$$J_{E,EM}^\mu = \langle -(b^2 u^\mu u_t - b^\mu b_t + \delta_t^\mu b^2 / 2) \rangle, \quad (26)$$

$$J_{E,FI}^\mu = \langle -(\rho + u + p_g) u^\mu u_t - \delta_t^\mu p_g \rangle,$$

where  $\delta_\nu^\mu$  is the Kronecker delta and  $\langle \dots \rangle$  denotes an average over  $t$  and  $\phi$ . Unlike Equation 22, we do not consider a density-weighted average here. Previous studies that investigate the transport of angular momentum in global accretion flows further breakdown the electromagnetic and fluid contributions of  $J_L^\mu$  into a laminar and turbulent component (Béthune et al. 2017; Mishra et al. 2020; Jacquemin-Ide et al. 2021; Manikantan et al. 2023; Scepi et al. 2023; Jacquemin-Ide et al. 2024) or an advective and stress component (Penna et al. 2010; Chatterjee & Narayan 2022). In this study we restrict our analysis to the *total* electromagnetic and fluid portion as defined in Equation 25.

The partitioning of  $\mathfrak{J}_L$  and  $\mathfrak{J}_E$ , as defined in Equations 25 and 26, is plotted in Figure 11 for MAD  $a_* = +0.94$ . Significant efflux of electromagnetic angular momentum and energy in the jet, following the parabolic profile shown in the total currents respectively, supports BZ mechanism. This is seen clearly in the top two rows of Figure 13 where we plot the radial components of the currents for the same model as a function of colatitude  $\theta$ . The shift in the peak toward higher latitudes with increasing radius highlights the collimated structure of the jet.

Figure 12 is identical to Figure 11 but for SANE  $a_* = +0.5$ . We see that the conserved currents are directed radially inward across all latitudes implying the absence

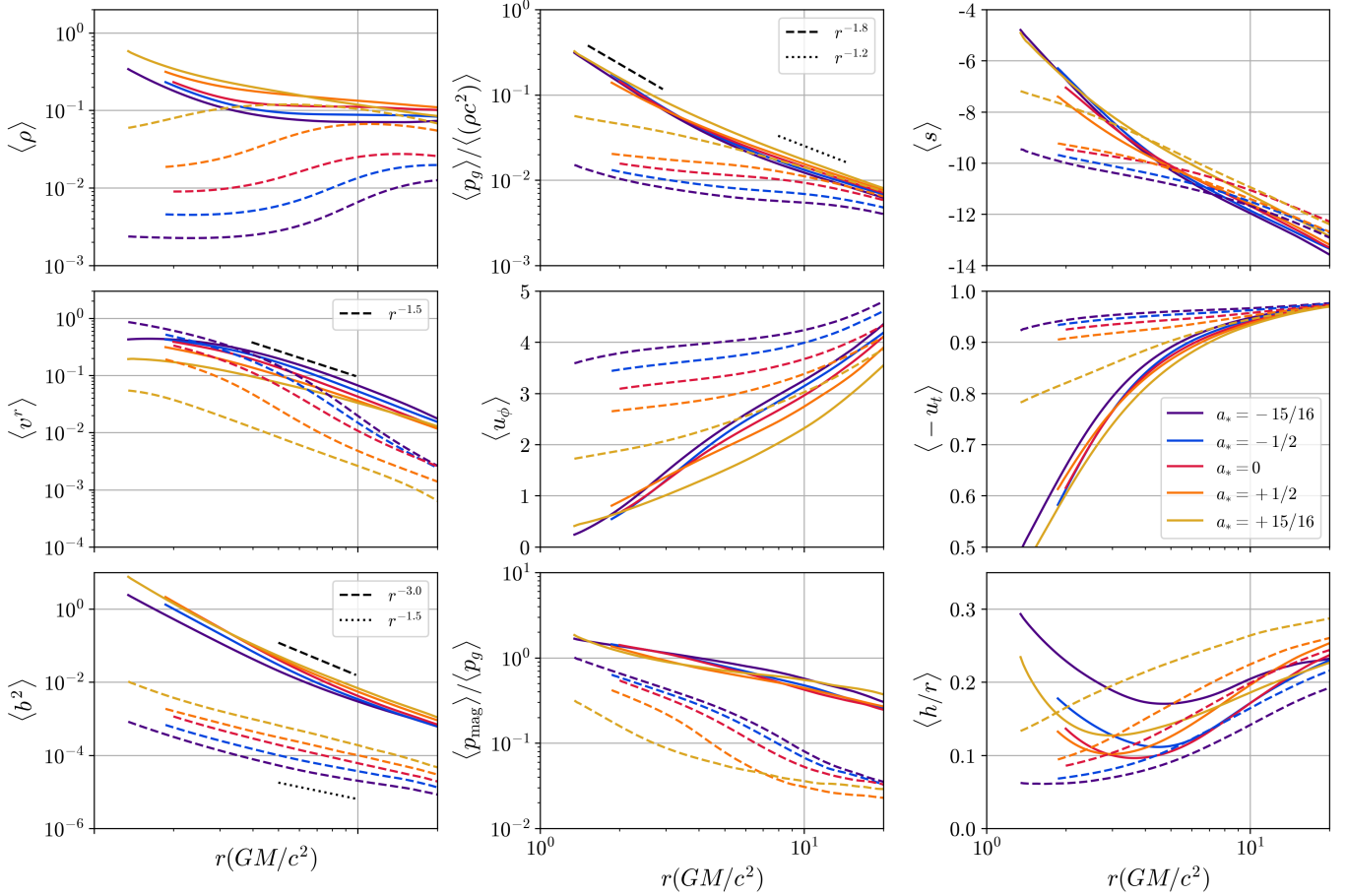


**Figure 9.** Radial profiles of rest-mass density  $\rho$  (in arbitrary code units), fluid temperature  $\Theta \equiv p_g/(\rho c^2)$ , fluid entropy  $s$ , radial velocity  $v^r$ , specific angular momentum  $u_\phi$ , specific energy  $u_t$ , magnetic field strength squared  $b^2$ , inverse plasma-beta  $\beta_p^{-1} \equiv (b^2/2)/p_g$ , and the density scale height  $h/r$ . The solid (dashed) lines represent MAD (SANE) simulations. Different colors correspond to different spins. Note that the units of rest-mass density in our simulations are arbitrary—a consequence of the scale-free nature of ideal GRMHD simulations—and therefore the absolute values of  $\langle \rho \rangle$  mean little. One should instead focus on the structure of the radial profile.

of any significant outflow<sup>13</sup>. The fluid component of the angular momentum and energy currents emphasizes the advective nature of the flow, while magnetic stresses facilitate outward transport of angular momentum in the disk through the MRI. The colatitude plots in Figure 13 underscores this point.

Finally, in Figure 14 we compare  $\mathfrak{J}_L$  and  $\mathfrak{J}_E$  across all simulations in our library by plotting  $\mathfrak{J}^r(\theta)$  at  $r = 10 r_g$ . In the MAD models, the outward transport of angular momentum and Poynting flux in the magnetically dominated jet shows a strong dependence on black hole spin. Note that negative values for  $\mathfrak{J}^r$  in the jet for retrograde models result from the corotation of the magnetic field

and plasma with the black hole, i.e.,  $u_\phi < 0$  (see Wong et al. 2021).  $\mathfrak{J}^r(\theta)$  shows a weak dependence on black hole spin for SANE models.

#### 4.5. Jet power

Global simulations of black hole accretion produce relativistic outflows of highly magnetized material “jets” along the black hole spin axis (see e.g., McKinney & Gammie 2004; Tchekhovskoy et al. 2011; also see Davis & Tchekhovskoy 2020; Komissarov & Porth 2021 for a recent review of jets in numerical simulations)<sup>14</sup>. These jets are consistent with the Blandford-Znajek picture

<sup>13</sup> While there is some outflow in  $\mathfrak{J}_L$  close to the poles, the colorscale, which plots the magnitude of poloidal components of the current, suggests this is negligible (recall the colorscale is logarithmically spaced).

<sup>14</sup> The picture is less clear for tilted accretion flows, where the angular momentum vector of disk is not necessarily aligned with that of the black hole. Liska et al. (2018); Chatterjee et al. (2020) find the jet aligns with the disk’s angular momentum vector, while Ressler et al. (2023) observe the jet aligned with the black hole spin axis in the case of MAD accretion flows.

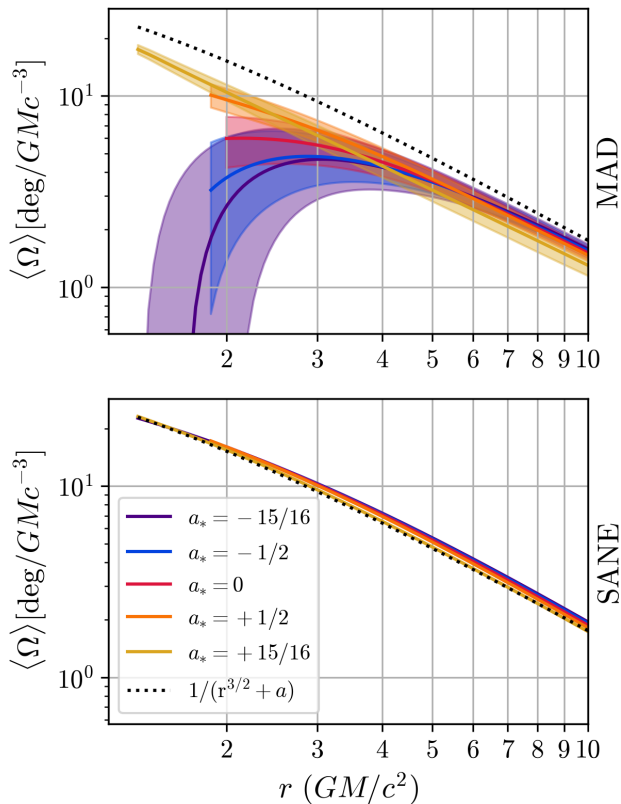


**Figure 10.** Angular velocity profiles  $\langle \Omega \rangle \equiv \langle u^\phi \rangle / \langle u^t \rangle$  in Kerr-Schild coordinates in units of  $\text{deg}/GM/c^3$ . The solid line plots the time-average value and the shaded region plots one standard deviation. The dotted black line is the Keplerian fit  $\Omega_K = (r^{3/2} + a)^{-1}$  for  $a_* = +0.94$ . The MAD rotational profiles are sub-Keplerian and have a significantly greater spread as compared to the SANE models. The SANE angular velocity agrees with the Keplerian expectation.

where the field lines that are brought in by the accreting plasma are dragged by the black hole in its ergosphere before eventually being launched carrying energy and momentum outward.

Although there is a qualitative understanding of the morphology of a typical black hole accretion system (see Figure 1 in Porth et al. 2019), there is no consensus on how one quantitatively defines the jet. McKinney & Gammie (2004) use the geometric Bernoulli parameter  $-u_t$ , while Narayan et al. (2012); Mościbrodzka et al. (2014) prefer a fluid Bernoulli parameter to classify outflows. There is also the MHD Bernoulli parameter (Penna et al. 2013; Yuan et al. 2015) that includes the magnetic energy contribution. Narayan et al. (2012) consider the ratio of total energy flux to the rest-mass flux  $\mu \equiv T_t^r / (\rho u^r) - 1$ . In this work we follow EHTC M87 V, where the jet is the region (within 1 ra-

dian of the pole) that satisfies,

$$(\beta\gamma)^2 \equiv \left( \frac{-T_t^r}{\rho u^r} \right)^2 - 1 > (\beta\gamma)_{\text{cut}}^2, \quad (27)$$

where  $-T_t^r$  and  $\rho u^r$  are time- and azimuth-averaged.  $(\beta\gamma)_{\text{cut}}$  is set to unity but the choice of the cut is arbitrary and Figure 10 in EHTC M87 V explores the effect of changing this value. The total mechanical power in the relativistic jet is then defined as,

$$P_{\text{jet}} = \int_{\beta\gamma > (\beta\gamma)_{\text{cut}}} d\theta \frac{1}{\Delta t} \int dt d\phi \sqrt{-g} (-T_t^r - \rho u^r). \quad (28)$$

measured at  $r = 100 r_g$ . Additionally, we also define a total outflow power  $P_{\text{out}}$  that is computed in the same manner as Equation 28 but without the  $(\beta\gamma)_{\text{cut}}$ . The  $\theta$  integral is instead carried out over 1 radian about the poles. This diagnostic includes both the fast-moving collimated jet, and the slow-moving winds further away from the poles. To give a sense for the various definitions of a jet in the literature, we plot these cuts in Figure 15.

We report jet and outflow power for the v3 library in Table 3. We see that according to our definition of  $P_{\text{jet}}$ , low spinning SANEs do not produce an appreciable jet, but do contain slow outgoing winds that result in a non-zero  $P_{\text{out}}$ . MAD  $a_* = +0.94$  has the most powerful jet, an outcome that is expected if the driving mechanism is the Blandford-Znajek process (where  $P_{\text{jet}} \propto a_*^2 \Phi_{\text{BH}}^2$ ; see e.g. McKinney 2005; Tchekhovskoy et al. 2010). Finally, we note that for models where  $P_{\text{jet}} \neq 0$ , this quantity is dominated by the Poynting flux.

#### 4.6. Black hole spin-up/spin-down

Bardeen (1970) was the first to consider the role of the surrounding environment on the properties of the central black hole. He assumed a cold equatorial accretion disk with matter plunging from the ISCO onto the black hole. He showed that this leads to the black hole achieving the maximal spin  $a_* = 1$  in finite time. Thorne (1974) included the effect of radiation emitted from the disk on the spin-up of the black hole. The photons captured by the black hole provide a counteracting torque that allows a maximal spin-up of  $a_* \simeq 0.998$ . The author highlights the assumptions in their model, particularly regarding the potential sensitivity of the results to the disk thickness ( $h/r$ ) and the presence of local magnetic fields.

Gammie et al. (2004) used GRMHD simulations to address the question of black hole spin-up. They considered axisymmetric SANE simulations to identify spin equilibrium (defined as  $s = 0$ ; see also Shapiro 2005) where,

$$s \equiv \frac{da_*}{dt} \frac{M}{\dot{M}}. \quad (29)$$

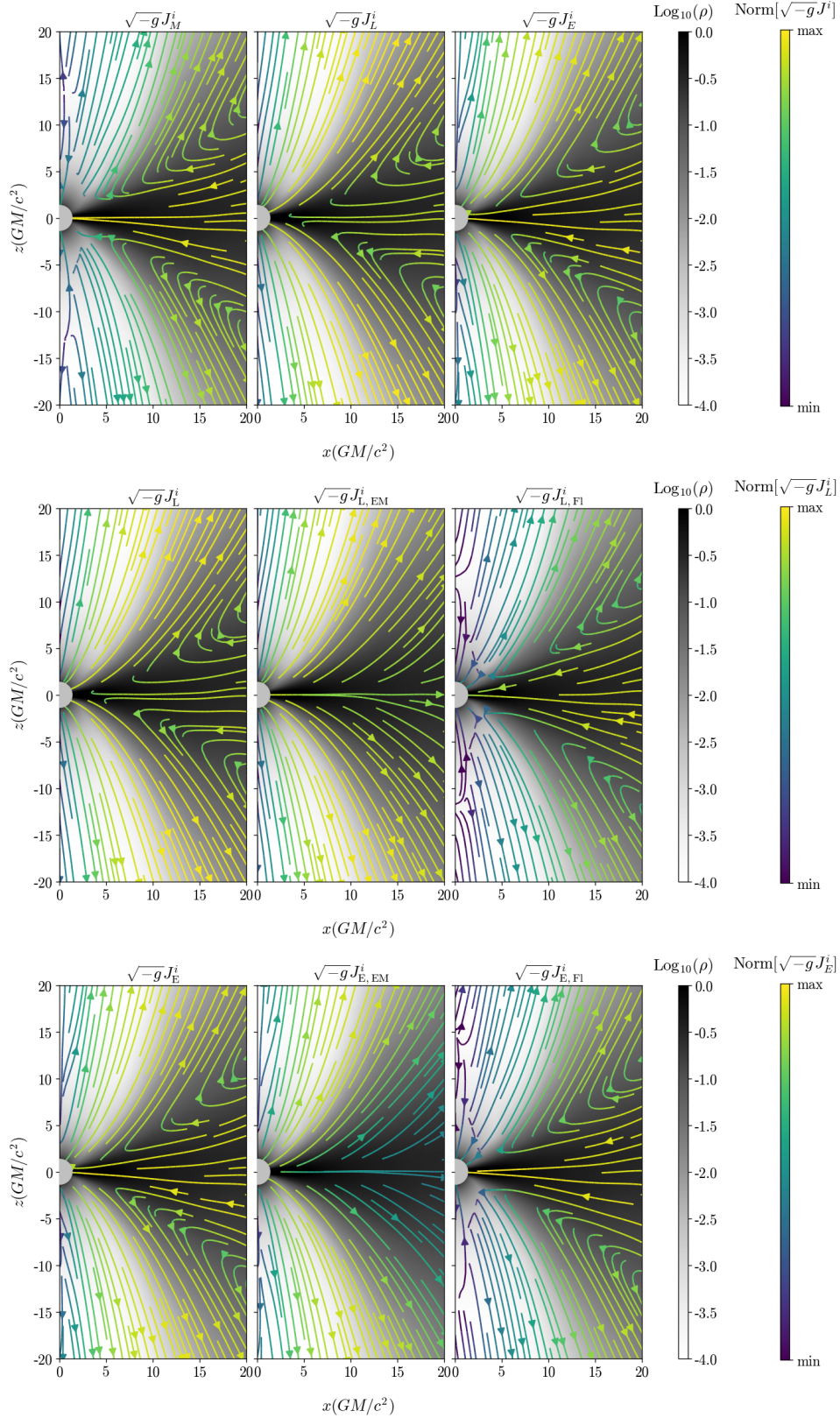


**Figure 11.** Time- and azimuth-averaged poloidal slices of rest-mass density with averaged conserved currents overlaid for the MAD  $a_* = +0.94$  model. In the top row we plot (left to right) the mass  $\mathfrak{J}_M \equiv \sqrt{-g}\rho u^\mu$ , angular momentum  $\mathfrak{J}_L \equiv \sqrt{-g}T_\phi^\mu$ , and energy  $\mathfrak{J}_E \equiv -\sqrt{-g}T_t^\mu$  currents. The middle row shows from left to right the total angular momentum current, the electromagnetic contribution, and the fluid contribution respectively. The bottom row is similar to the middle row except we plot the energy current. The arrows in the flow lines indicate the direction of the conserved currents and the colorscale indicates the magnitude plotted on a logscale since it can vary by several decades on a poloidal slice. The general morphology of the currents is similar, namely, strong inflow in the disk that transitions to an outflow at higher latitudes.



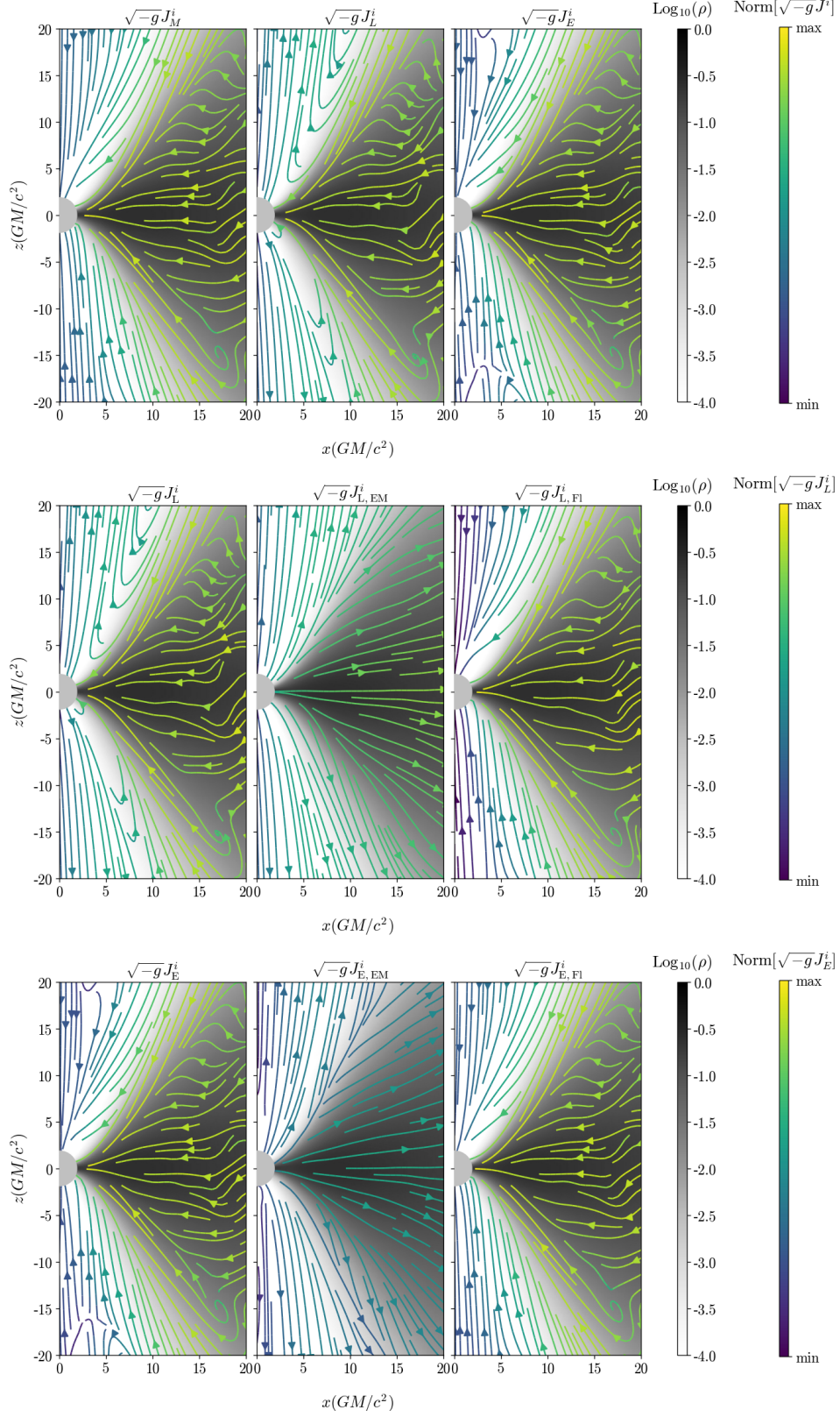


**Figure 12.** Same as Figure 11 but for SANE  $a_* = +0.5$

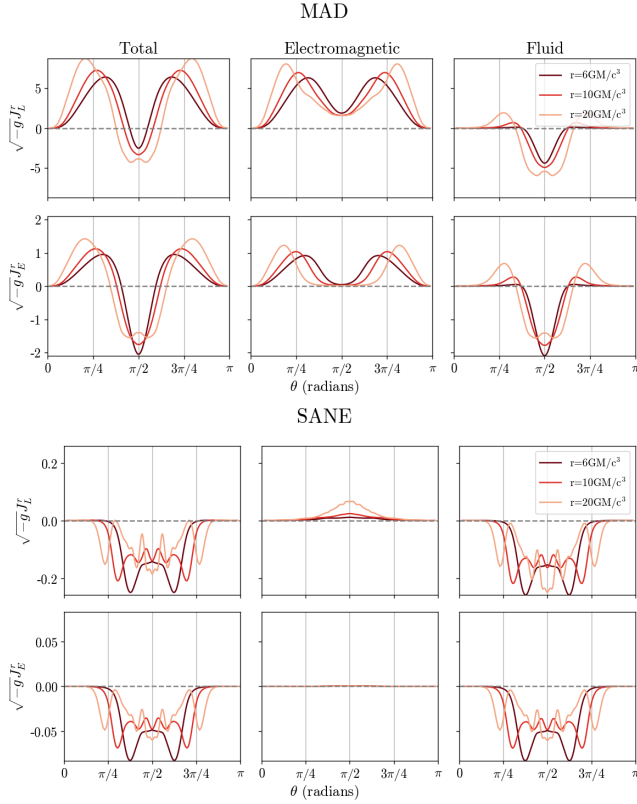


**Figure 13.**  $\mathfrak{J}_L$  and  $\mathfrak{J}_E$  colatitude dependence at three radii  $r = 6, 10, 20 r_g$ . The top (bottom) two rows corresponds to the simulation shown in Figure 11 (Figure 12). For each simulation we show in the top (bottom) row the angular momentum (energy) current. The left column plots the *total* current, while the middle and right columns plot the electromagnetic and fluid contribution respectively. In the MAD simulation we see outward transport of energy and angular momentum flux in the jet carried by the collimated magnetic fields; while the fluid stresses are inward and peak in the disk. The total current closely resembles the fluid sector profile for the SANE simulation with some outward electromagnetic angular momentum flux in the disk.

This may be expressed in terms of the ingoing specific angular momentum and energy flux as,

$$s = l - 2a_*e. \quad (30)$$

They find spin equilibrium at  $a_* \simeq 0.94$ . [Teukhovskoy et al. \(2012\)](#) and more recently [Narayan et al. \(2022\)](#); [Lowell et al. \(2024\)](#) found the spin equilibrium in MAD simulations is significantly lower, with  $a_{\text{eq}} \lesssim 0.1$ . This is attributed to strong magnetic fields in the jet, which extract angular momentum from the black hole more efficiently than that supplied by disk.

In Figure 16 we plot the time-averaged spin-up parameter. We see that the SANE simulations, where the magnetic fields are dynamically unimportant and primarily serve to transport angular momentum outward

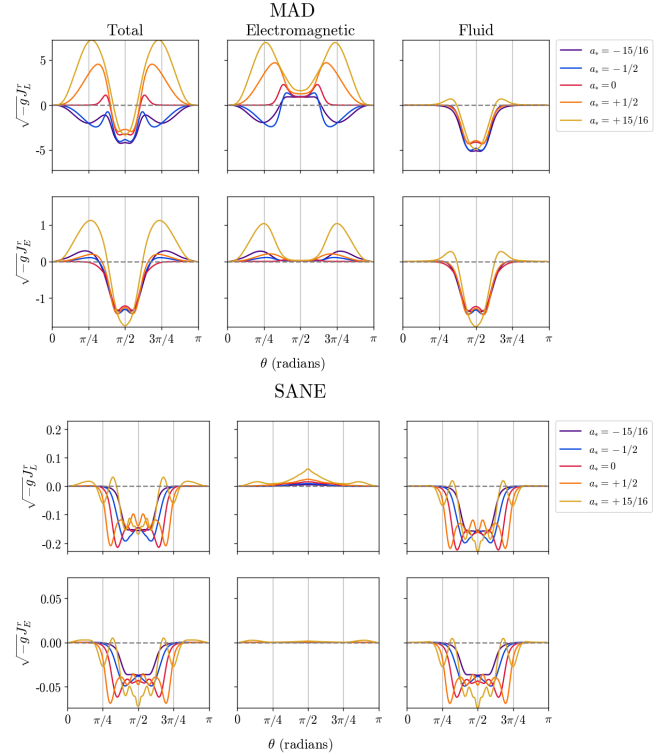


**Figure 14.** Similar to Figure 13, but instead we plot the conserved current profiles at a fixed radius  $r = 10 r_g$  for all simulations in the library. The outward transport of angular momentum and energy in the jet strongly depends on the black hole spin for the MAD models. Negative values of  $\sqrt{-g}J_L^z$  at higher latitudes for the retrograde models is simply a reflection of the magnetic fieldlines and plasma in the jet corotating with the black hole.

**Table 3.** Jet power statistics

Flux	$a_*$	$P_{\text{jet}}/(\dot{M}c^2)$	$P_{\text{out}}/(\dot{M}c^2)$	$P_{\text{jet,em}}/P_{\text{jet}}$
MAD	-15/16	$3.50 \times 10^{-1}$	$3.83 \times 10^{-1}$	$7.22 \times 10^{-1}$
MAD	-1/2	$9.08 \times 10^{-2}$	$1.27 \times 10^{-1}$	$7.83 \times 10^{-1}$
MAD	0	$6.02 \times 10^{-5}$	$2.27 \times 10^{-2}$	$6.10 \times 10^{-1}$
MAD	+1/2	$1.97 \times 10^{-1}$	$2.49 \times 10^{-1}$	$8.18 \times 10^{-1}$
MAD	+15/16	1.51	1.60	$7.11 \times 10^{-1}$
SANE	-15/16	$2.15 \times 10^{-3}$	$2.46 \times 10^{-3}$	$7.64 \times 10^{-1}$
SANE	-1/2	0.00	$3.53 \times 10^{-4}$	-
SANE	0	0.00	$3.96 \times 10^{-4}$	-
SANE	+1/2	0.00	$8.37 \times 10^{-4}$	-
SANE	+15/16	$3.30 \times 10^{-2}$	$4.32 \times 10^{-2}$	$6.45 \times 10^{-1}$

NOTE—Summary of jet and outflow power. The first two columns are identical to Table 1 where Flux labels the strength of the magnetic field at the horizon and  $a_*$  is black hole spin. The third and fourth column are jet and outflow efficiencies respectively, and the final column is the electromagnetic fraction of the jet power.

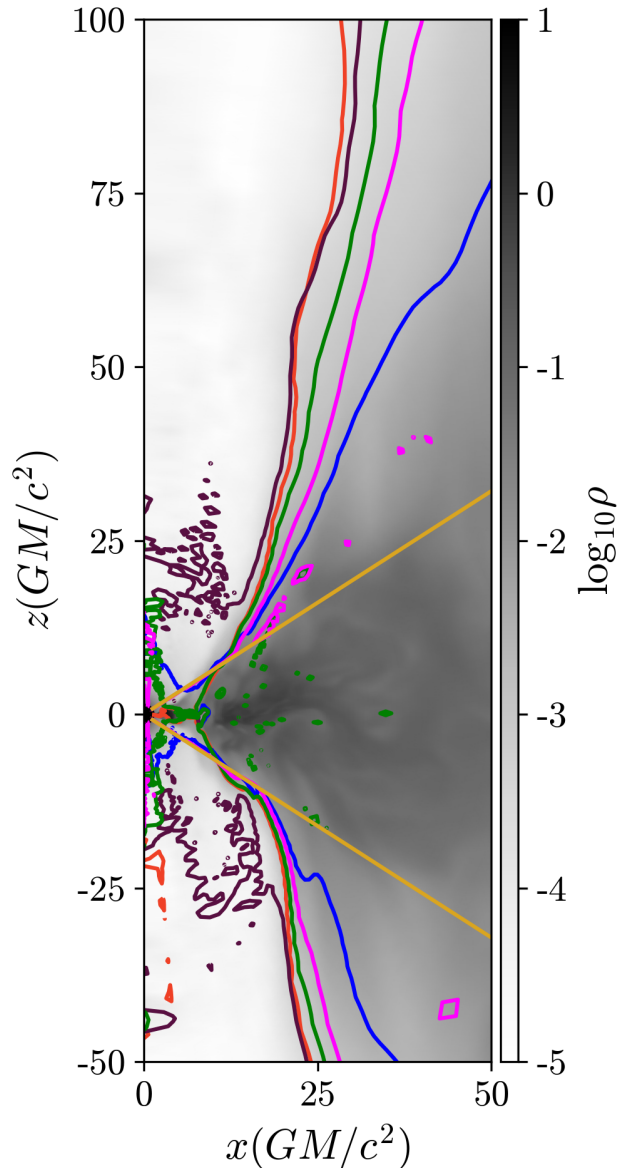


**Figure 15.** A poloidal cut of a MAD simulation illustrating various definitions of a jet or outflow. The background color saturation represents rest-mass density in code units. The goldenrod lines mark geometric boundaries at  $\theta = 1$  and  $\theta = \pi - 1$ , which are used in this work to compute the total outflow power  $P_{\text{out}}$ . The blue line is the  $-u_t = 1$  contour, while the magenta line represents  $\beta\gamma = 1$ , the latter serving as the jet definition in this study. The green, plum, and red lines indicate contours where  $\mu = 1$ ,  $\text{Be} = 1$  (fluid Bernoulli parameter), and  $\sigma = 1$ , respectively.

through the disk, closely follow the thin disk expectation,

$$s_{\text{thin}} = l_{\text{isco}} - 2a_*e_{\text{isco}}. \quad (31)$$

However, the role of magnetic fields is not ignorable as the models achieve spin equilibrium at  $a_{\text{eq}} \sim 0.94$ , con-

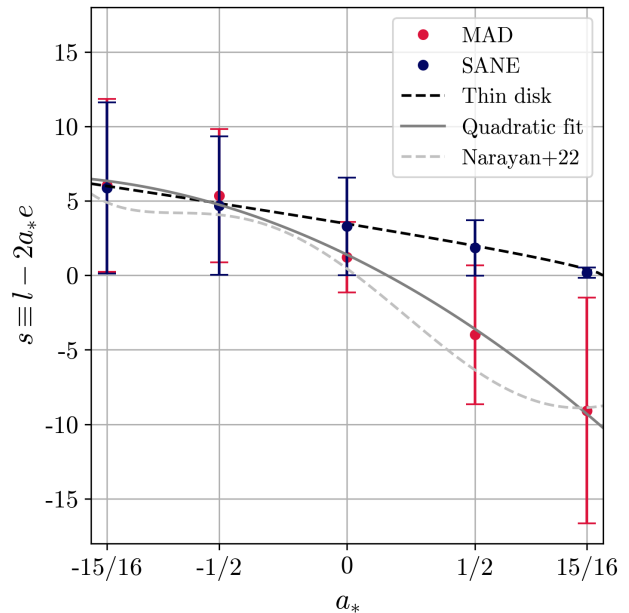


**Figure 16.** The spin-up parameter ‘ $s$ ’ given by Equation 30. The markers indicate the time-averaged value and error bars represent  $1\sigma$ . Red and blue markers are MAD and SANE simulations respectively. The black dashed line is the expected thin disk values (Equation 31). The solid gray line is the quadratic fit (Equation 32) and the dashed silver line is the fifth-order polynomial fit provided in Narayan et al. (2022).

firming earlier work. Prograde MAD models possess a negative spin-up parameter indicating black hole spin-down. The spin-down is stronger for more rapidly spinning black holes due to the presence of stronger radial magnetic fields anchored at the event horizon. We provide a quadratic fit to our models,

$$s_{\text{fit}} = -3.267a_*^2 - 8.349a_* + 1.387, \quad (32)$$

and also plot the fifth-order fit from Narayan et al. (2022)<sup>15</sup>. The retrograde models spin up the black hole; however, since  $a_* < 0$  for these models, the absolute value of spin decreases. Finally, we observe that the time variation in  $s$  (indicated by the errorbars) is more pronounced for MADs, likely due to the intermittent nature of accretion flow in these simulations.

## 5. SIMULATION DATA PRODUCTS

The v3 GRMHD simulations are staged on a local file server at the University of Illinois at Urbana-Champaign. Interested readers may access the data

<sup>15</sup> Note that our sampling of the black hole spin space is sparser than Narayan et al. (2022), and we consider a lower order polynomial for our fit.

using the following URL: <http://thz.astro.illinois.edu/>. A Python package for analyzing the GRMHD data is publicly available<sup>16</sup>. Due to constraints on storage space, we host simulation snapshots corresponding to 25,000 – 30,000  $t_g$ , but the full dataset will be shared upon reasonable request to the corresponding author.

## 6. SUMMARY

In this paper we present data products from a suite of ideal GRMHD simulations of black hole accretion. The library consists of 10 simulations that cover the accretion disk magnetization state ‘ $\phi_b$ ’, black hole spin ‘ $a_*$ ’ parameter space. We consider 5 spins  $a_* = 0, \pm 0.5, \pm 0.94$  for each state of magnetization (MAD and SANE). The GRMHD simulations discussed in this paper were used in the Galactic center analysis by the EHT (EHTC SgrA V; EHTC SgrA VIII) and in other works (Georgiev et al. 2022; Conroy et al. 2023; Chan et al. 2024; Chan & Chan 2024; Joshi et al. 2024). We studied trends across the simulations and summarize our findings below:

1. The horizon-penetrating, normalized radial angular momentum flux in SANE simulations closely matches the thin-disk expectation. In prograde MAD simulations, magnetic field lines anchored at the horizon extract angular momentum from the black hole, and this overwhelms the inflow of positive angular momentum from the disk. This result is consistent with the findings of the “spin-up” study, where prograde MAD models experience spin-down, i.e., a reduction in the black hole’s angular momentum. SANE models follow the thin-disk expectation closely and achieve spin equilibrium at  $a_* \approx 0.94$ .
2. For  $a_* \gtrsim 0$ , the thermodynamic component of the specific energy flux is no longer negligible in the SANE simulations, and the total specific energy flux for prograde models exceeds the thin disk expectation. This is further evidenced by Figure 9, which shows an increase in fluid temperature near the black hole with increasing spin. The  $a_* = +0.94$  MAD model has an outflow efficiency  $> 1$ , indicating that the energy outflow in jets exceeds the energy supplied by the accretion disk.
3. Analysis of the time series of radial fluxes at the horizon reveals that MAD simulations exhibit greater variability on average than their SANE

counterparts. This aligns with the physical picture in which MAD disks undergo aperiodic flux eruption events, characterized by a drop in  $\Phi_{\text{BH}}$  and a subsequent rise in  $\dot{M}$ , whereas SANE accretion is more uniform. For both SANE and MAD simulations we find that the average  $\dot{M}$  variability increases with spin for prograde models, but is independent of spin for retrograde models, consistent with the findings of Narayan et al. (2022).

4. A time- and azimuth-averaged study of the accretion disk shows that MAD disks are consistently hotter than SANE disks within  $r \lesssim 10 r_g$ . Prograde MAD models produce more powerful and wider jets than their retrograde counterparts, resulting in narrower disks for retrograde models. We find the spin-dependence of temperature, specific angular momentum  $u_\phi$ , and disk scale height  $h/r$  in SANE simulations closely aligns with the semi-analytic model of relativistic, advection-dominated viscous accretion flow provided by Popham & Gammie (1998). Additionally, MAD disks are sub-Keplerian with significantly larger variance in angular velocity as compared to SANE disks.
5. We examine the transport of mass, angular momentum, and energy in our simulations by analyzing conserved currents  $J_M = \rho u^\mu$ ,  $J_L = T_\phi^\mu$ , and  $J_E = -T_t^\mu$  respectively. In MAD simulations, dynamically significant magnetic fields facilitate the outward transport of angular momentum and energy through the jet and winds. Within the disk, the fluid sector primarily drives the inward transport of angular momentum and energy. In SANE simulations, the electromagnetic component contributes to outward angular momentum transport within the disk, indicating the influence of MRI.

Finally, it is worth providing an honest assessment of the limitations of this work. This is in addition to the caveats associated with ideal GRMHD discussed in Section 2.2. The spatial resolution of the simulations in the v3 library is somewhat lower than contemporary studies<sup>17</sup>. Resolution studies indicate that while time-averaged, bulk properties of MAD accretion flows are converged at this resolution (White et al. 2019; Salas et al. 2024), the spatial structure of the flow at higher

<sup>16</sup> <https://github.com/AFD-Illinois/pyharm/>

<sup>17</sup> Due to the series of transformation made to the KS coordinates (Section 3.3) that increase the effective resolution in the midplane and close to the black hole, a comparison solely based on number of grid zones may be misleading.

latitudes, such as the jet-disk boundary, is not converged. This can be important when interpreting VLBI observations of edge-brightened jets (Walker et al. 2018; Kim et al. 2018; Lu et al. 2023; Davelaar et al. 2023; Kim et al. 2024). In SANE simulations, where the MRI facilitates outward transport of angular momentum, Shiohara et al. (2012); Porth et al. (2019) find that the  $\alpha$ -parameter does not converge over the range of resolutions considered. Additionally, Ripperda et al. (2022) find higher-resolution simulations necessary to achieve convergence in the magnetic reconnection rate.

To minimize differences in synthetic observables arising from code-dependent choices, we chose  $\hat{\gamma} = 4/3$  to be consistent with other GRMHD codes considered in EHTC SgrA V. The lack of an efficient coupling mechanism between the ions and electrons in RIAFs results in a two-temperature plasma with relativistic electrons and nonrelativistic ions. This suggests that in single-temperature simulations, the fluid adiabatic index should be close to  $5/3$  (C. F. Gammie 2024, in prep).

Although this library evolves simulations for a significantly extended period compared to previous studies used in EHT analysis (Wong et al. 2022), even longer runs will be necessary to achieve inflow equilibrium at larger radii. This may be crucial as Faraday rotation effects arising from outer regions of the accretion disk can undermine polarimetric images. Finally, a finer sampling of black hole spin, i.e., an increased number of GRMHD simulations with different  $a_*$ , may provide an independent constraint on black hole spin (V. Bernsheyn et al. 2024, in prep).

## ACKNOWLEDGMENTS

V.D. is grateful to Abhishek Joshi for discussions that greatly improved the quality of certain sections in this text. V.D. was supported in part by the ICASU/NCSA Fellowship. G.N.W. was supported by the Taplin Fellowship and the Princeton Gravity Initiative. This work was supported by NSF grants AST 17-16327 (horizon), OISE 17-43747, and AST 20-34306. This research used resources of the Oak Ridge Leadership Computing Facility at the Oak Ridge National Laboratory, which is supported by the Office of Science of the U.S. Department of Energy under Contract No. DE-AC05-00OR22725. This research used resources of the Argonne Leadership Computing Facility, which is a DOE Office of Science User Facility supported under Contract DE-AC02-06CH11357. This research is part of the Delta research computing project, which is supported by the National Science Foundation (award OCI 2005572), and the State of Illinois. Delta is a joint effort of the University of Illinois at Urbana-Champaign and its National Center for Supercomputing Applications. The data analysis was possible thanks to the high throughput computing utility ‘Launcher’ (Wilson 2017). This work used the Extreme Science and Engineering Discovery Environment (XSEDE), which is supported by National Science Foundation grant number ACI-1548562, specifically the XSEDE resources Longhorn, Frontera, and Stampede2 at the Texas Advanced Computing Center (TACC) through allocation TG-AST170024. The authors acknowledge the Texas Advanced Computing Center (TACC) at The University of Texas at Austin for providing computational resources that have contributed to the research results reported within this paper.

## APPENDIX

### A. CALCULATING THE MAGNETIC FLUX THREADING THE BLACK HOLE HORIZON

The standard approach for calculating the magnetic flux at the event horizon is given by Equation 12. This approach assumes that the total flux crossing each hemisphere of the horizon—north ( $\theta < \pi/2$ ) and south ( $\theta \geq \pi/2$ )—is equal in magnitude and opposite in direction. However, this assumption may not hold if the magnetic field changes direction in certain regions within either hemisphere.

To investigate this, we compute the magnetic flux across the northern and southern hemispheres using the

following definitions:

$$\Phi_{\text{BH}}^{\text{N}} = \int_{\phi} \int_{\theta < \pi/2} B^r \sqrt{-g} \, d\theta \, d\phi, \quad (\text{A1})$$

$$\Phi_{\text{BH}}^{\text{S}} = \int_{\phi} \int_{\theta \geq \pi/2} -B^r \sqrt{-g} \, d\theta \, d\phi, \quad (\text{A2})$$

and compare them with the standard definition. The negative sign in Equation A2 ensures that  $\Phi_{\text{BH}}^{\text{N}}$  and  $\Phi_{\text{BH}}^{\text{S}}$  are consistent.

In Figure 17 we plot  $\phi_b$  using Equations 12, A1, and A2. The flux across both the hemispheres (Equations A1 and A2) agrees closely for all the models, with relative differences being less than  $10^{-6}$ . The standard definition of the flux emulates the hemispherical values

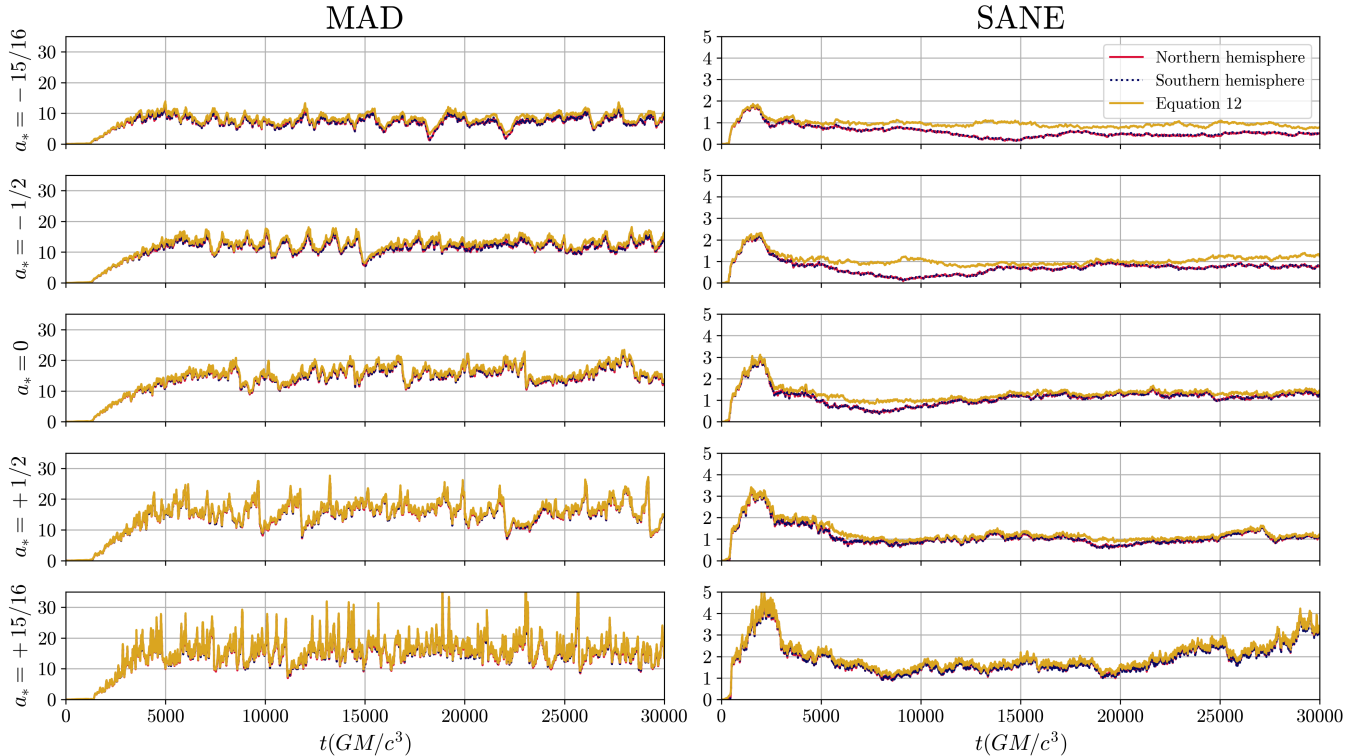


**Figure 17.** A time series of the dimensionless magnetic flux crossing the event horizon for all the models in `v3`. Columns: Left: MAD, Right: SANE simulations. Rows: Top to bottom: Increasing spin from  $a_* = -15/16$  to  $a_* = +15/16$ . The gray line plots the flux as computed according to Equation 12, while the goldenrod and magenta lines plot  $\Phi_{\text{BH}}^{\text{N}}$  (Equation A1) and  $\Phi_{\text{BH}}^{\text{S}}$  (Equation A2) respectively.

for all MAD simulations and prograde SANE models. However, for  $a_* \leq 0$  SANE models this is not the case, and at several points in the simulation the standard calculation overestimates the individual hemispherical flux estimates.

To better understand this, we plot the radial component of the magnetic field  $B^r$  for two models: one where the values do not match, SANE  $a_* = -0.5$  (Figure 18), and one where they do, SANE  $a_* = +0.5$  (Figure 19). In the retrograde model we see a quadrupolar structure in  $B^r$  that persists over time. This polarity reversal within each hemisphere explains the reduced magnetic flux when computed using Equations A1 and A2 which accounts for the sign reversal. In contrast, for the prograde model, the time-averaged  $B^r$  maintains a constant sign in each hemisphere<sup>18</sup>.

<sup>18</sup> We observe a numerical artifact near the poles associated with meshblock boundaries in one of the simulations (SANE  $a_* = -0.94$ ). This issue has been resolved in KHARMA since the `v3` library was generated. We reran this simulation and confirmed that the artifact does not impact the bulk properties of the disk. The new simulation is also available at <http://thz.astro.illinois.edu/>.

## B. FAILURE MODES IN THE `v3` LIBRARY

In highly magnetized regions ( $\sigma \gg 1$  or  $\beta^{-1} \gg 1$ ) the fluid rest-mass and internal energy make up only a small fraction of the total energy. The truncation error incurred when evolving the components of the stress-energy tensor in these regions can lead to significant inaccuracies in the fluid primitives. Consequently, grid-based MHD codes are prone to numerical failures during primitive variable recovery when there is an unequal contribution to the energy budget. To avoid such failures and to prevent the code from crashing, fluid quantities are reset to predefined limits. Floors on rest-mass density  $\rho$  and internal energy  $u$  can be applied in several ways:

- “Geometrically”, where  $\rho_{\text{min}}$  and  $u_{\text{min}}$  are specified as a function of radius;
- By imposing ceilings on magnetic quantities  $\sigma$  and  $\beta^{-1}$ , which translate into minimum values for  $\rho$  and  $u$ ,
- By setting limits on thermodynamic quantities such as fluid temperature  $p_g/\rho$  or entropy  $\kappa_{\text{tot}} \equiv p_g/\rho^{\tilde{\gamma}}$ .

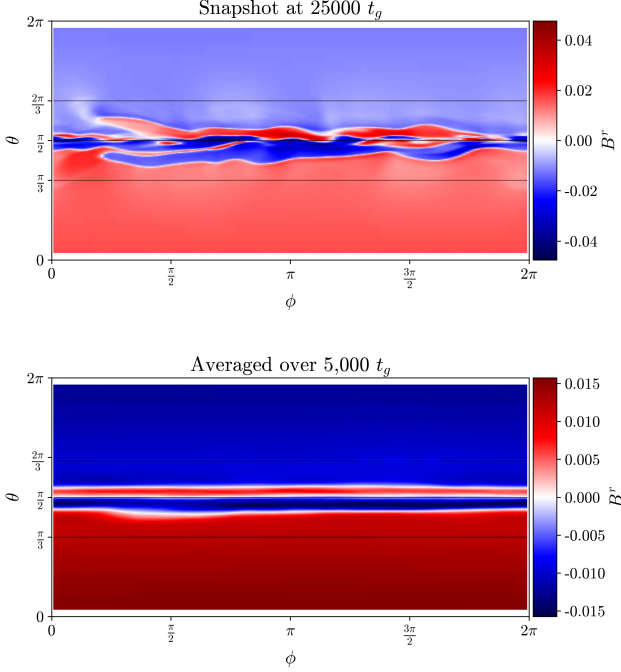


**Figure 18.** A heat map of the radial component of the magnetic field  $B^r$  at the event horizon for the SANE  $a_* = -0.5$  simulation. Top panel:  $B^r$  at a specific instant in time. Bottom panel:  $B^r$  averaged over the interval  $t = [25, 30] \times 10^3 t_g$ . In both panels, note that  $B^r$  changes polarity within each hemisphere. This behavior is not accounted for in Equation 12 leading to an overestimation of  $\Phi_{\text{BH}}$ .

Typically, a combination of these floor prescriptions is employed to maintain numerical stability while minimizing their effect on fluid evolution. Additionally, we restrict the Lorentz factor  $\Gamma$  to prevent superluminal speeds. In the v3 library we consider the following floors and ceilings:

- $\rho > \rho_{\min} r^{-3/2}$  and  $u > u_{\min} r^{-5/2}$ , where  $\rho_{\min} = 10^{-5}$  and  $u_{\min} = 10^{-7}$ ,
- $b^2/\rho < \sigma_{\max}$ , where  $\sigma_{\max} = 100$ ,
- $\kappa_{\text{tot}} < \kappa_{\max}$  where  $\kappa_{\max} = 3$ ,
- $\Gamma < \Gamma_{\max}$  where  $\Gamma_{\max} = 50$ .

Floors can be applied in various frames, e.g., the co-moving fluid frame (Gammie et al. 2003), the normal observer frame (McKinney et al. 2012), or the drift frame (Ressler et al. 2017). The choice of frame affects the stability of the scheme in highly magnetized regions. Fluid frame floors directly modify the rest-mass density and internal energy primitives and are typically less stable than those applied in the normal observer or drift frame.

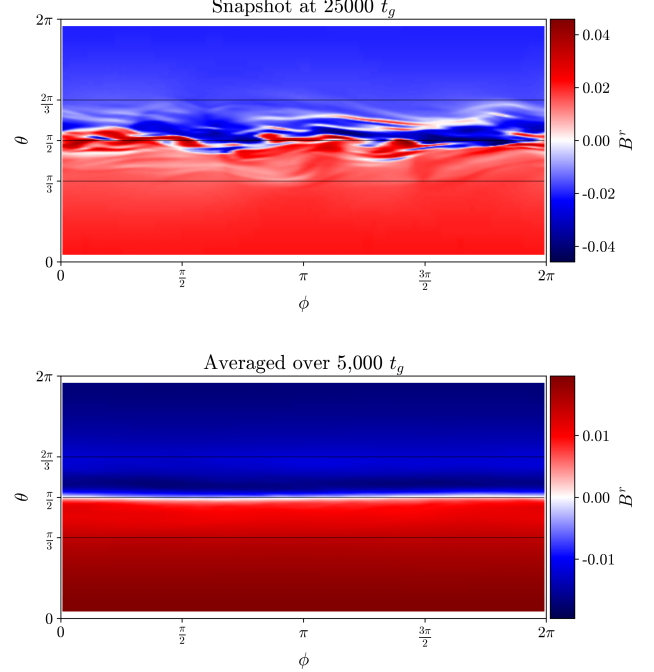


**Figure 19.** Same as Figure 18 but for SANE  $a_* = +0.5$ . The magnetic fields in this case are much more ordered, resulting in a consistent sign of  $B^r$  across both hemispheres.

In the v3 library, we inject material in the normal observer frame, which modifies the fluid conserved variables. This is followed by a  $\mathbf{U} \rightarrow \mathbf{P}$  operation for the floored grid zones. If any zone fails during the  $\mathbf{U} \rightarrow \mathbf{P}$  operation, KHARMA computes an average over adjacent zones where the primitives were successfully recovered.

In Figures 20 and 21 we show the time series of the fraction of total zones where the floors and ceilings are triggered for two of the models, MAD and SANE  $a_* = +0.5$  respectively. Initially, the magnetic field is confined to the FM torus, with only geometric floors activated in the regions outside the torus. As accretion begins, jets are launched, triggering the  $\sigma$  ceiling. MAD accretion flows produce powerful jets, with  $b^2/\rho \gg 1$  in the evacuated funnel region, explaining the larger fraction of zones reaching the  $\sigma$  ceiling in MAD simulations (see, e.g., Figure 22). For the chosen value of  $\kappa_{\max}$ , approximately 1% of the zones hit the entropy ceiling, which limits the internal energy in the funnel. Additionally, the ceiling on the Lorentz factor is primarily triggered in the MAD  $a_* = +0.94$  simulation, as high-spin MADs generate the most powerful jets (see Section 4.5), accelerating particle to large velocities in the funnel. Finally, we plot the fraction of zones where  $\mathbf{U} \rightarrow \mathbf{P}$

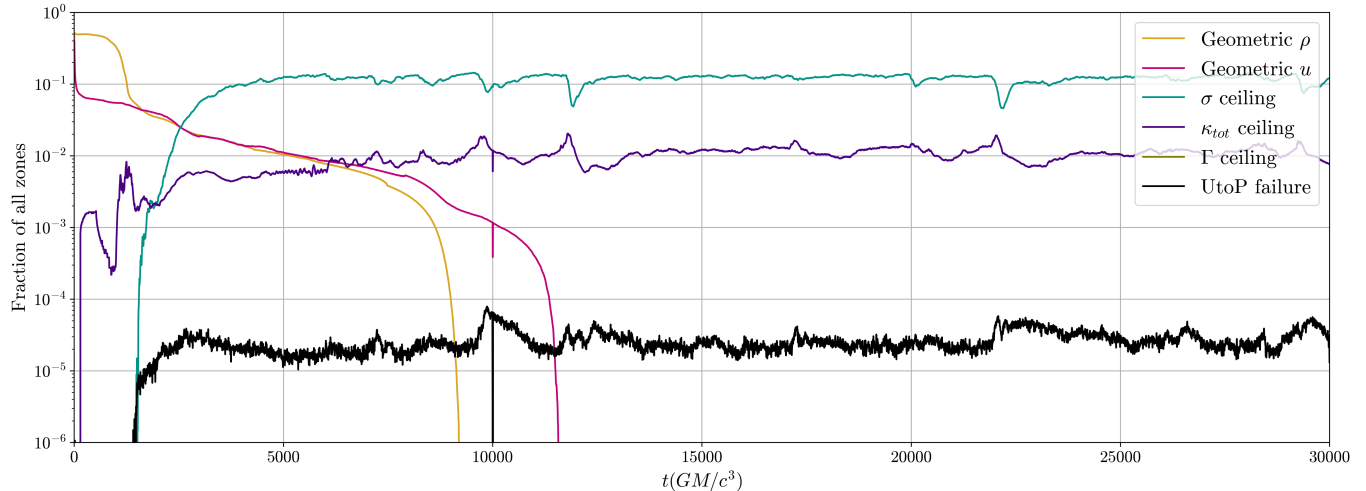


**Figure 20.** Time series of the fraction of total zones where floors and primitive recovery failures occur for MAD  $a_* = +0.5$ . Before accretion begins, geometric floors on  $\rho$  and  $u$  are the dominant contribution. As the evolution progresses and the funnel region becomes magnetically dominated,  $\sim 10\%$  of the zones have their rest-mass density set by a  $\sigma$  ceiling.

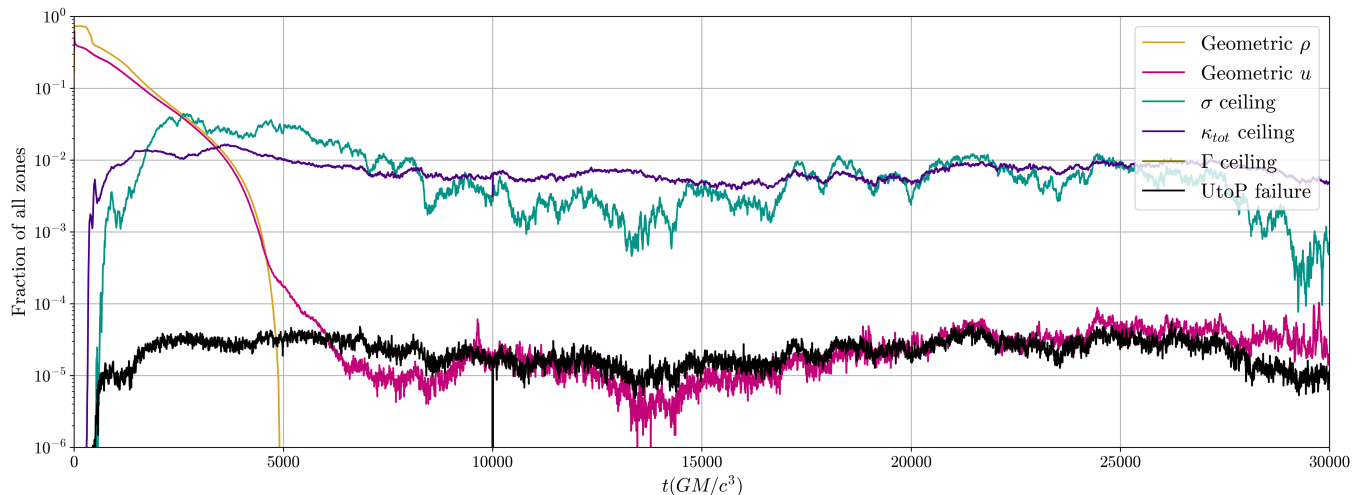


**Figure 21.** Similar to Figure 20, but for SANE  $a_* = +0.5$ . Compared to the MAD model, there are fewer flow hits, with the largest contributions coming from the entropy and  $\sigma$  ceilings.

fails and find that the failure rate is at a sub-percent level.

We conclude by highlighting several stability features introduced in KHARMA since the v3 library was generated, which reduces the use of floors and makes the code more robust in highly-magnetized regions. KHARMA now defaults to the primitive recovery scheme outlined in Kastaun et al. (2021), which guarantees convergence

to a valid and unique solution. This eliminates the need for a fixup routine and minimizes artificial modification to the fluid primitives. KHARMA now supports “first-order flux correction” (Beckwith & Stone 2011), which attempts a speculative step using higher-order reconstruction methods and reverts to a first-order reconstruction method in zones prone to floor application. This maintains the conservative nature of the scheme at the expense of some numerical dissipation.

## REFERENCES

Anile, A. M. 1990, *Relativistic Fluids and Magneto-fluids: With Applications in Astrophysics and Plasma Physics*, Cambridge Monographs on Mathematical Physics (Cambridge University Press), doi: [10.1017/CBO9780511564130](https://doi.org/10.1017/CBO9780511564130)

Anile, A. M., & Pennisi, S. 1987, *Annales de l’I.H.P. Physique théorique*, 46, 27. [http://www.numdam.org/item/AIHPA\\_1987\\_\\_46\\_1\\_27\\_0/](http://www.numdam.org/item/AIHPA_1987__46_1_27_0/)



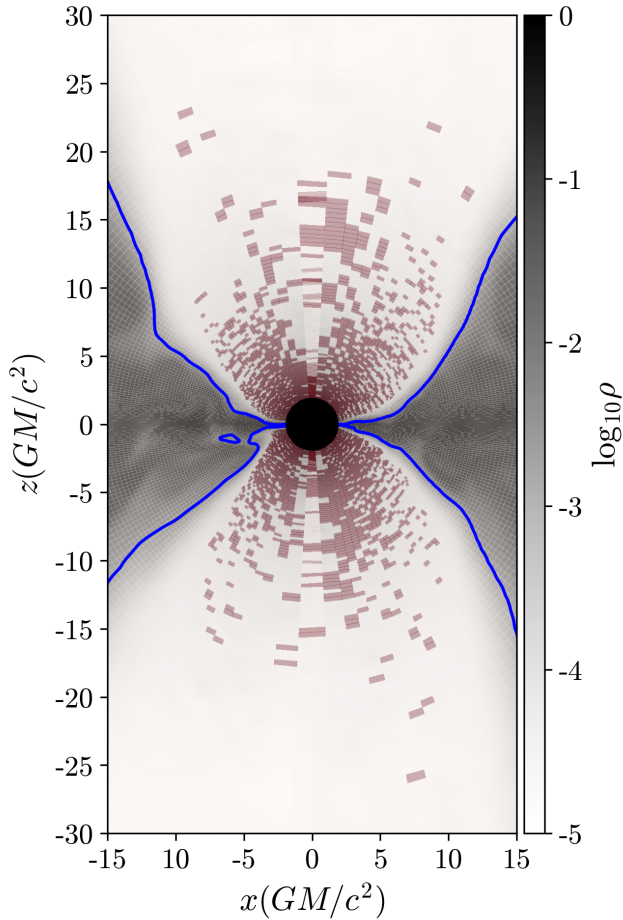


**Figure 22.** A snapshot from the MAD  $a_* = +0.5$  simulation. Grid zones where  $\sigma$  exceeds  $\sigma_{\max}$  are highlighted in red, while the blue contour indicates  $\sigma = 1$ . The underlying grayscale shading shows the logarithm of the rest-mass density in code units. The exponential radial coordinate focuses zones near the event horizon. Since  $\sigma$  peaks at the base of the jet, a substantial fraction of grid zones reach the  $\sigma$  ceiling in MAD simulations (see Figure 20).

Asada, K., & Nakamura, M. 2012, *ApJL*, 745, L28,  
doi: [10.1088/2041-8205/745/2/L28](https://doi.org/10.1088/2041-8205/745/2/L28)

Bacchini, F., Arzamasskiy, L., Zhdankin, V., et al. 2022,  
*ApJ*, 938, 86, doi: [10.3847/1538-4357/ac8a94](https://doi.org/10.3847/1538-4357/ac8a94)

Bacchini, F., Zhdankin, V., Gorbunov, E. A., et al. 2024,  
*PhRvL*, 133, 045202,  
doi: [10.1103/PhysRevLett.133.045202](https://doi.org/10.1103/PhysRevLett.133.045202)

Balbus, S. A., & Hawley, J. F. 1991, *ApJ*. . ., 376, 20

Bardeen, J. M. 1970, *Nature*, 226, 64,  
doi: [10.1038/226064a0](https://doi.org/10.1038/226064a0)

Bardeen, J. M., Press, W. H., & Teukolsky, S. A. 1972,  
*ApJ*, 178, 347, doi: [10.1086/151796](https://doi.org/10.1086/151796)

Beckwith, K., & Stone, J. M. 2011, *ApJS*, 193, 6,  
doi: [10.1088/0067-0049/193/1/6](https://doi.org/10.1088/0067-0049/193/1/6)

Béthune, W., Lesur, G., & Ferreira, J. 2017, *Astron.*

*Astrophys.*, 600, A75, doi: [10.1051/0004-6361/201630056](https://doi.org/10.1051/0004-6361/201630056)

Bisnovaty-Kogan, G. S., & Ruzmaikin, A. A. 1974,  
*Ap&SS*, 28, 45, doi: [10.1007/BF00642237](https://doi.org/10.1007/BF00642237)

—. 1976, *Astrophys Space Sci*, 42, 401,  
doi: [10.1007/BF01225967](https://doi.org/10.1007/BF01225967)

Blandford, R. D., & Znajek, R. L. 1977, *Monthly Notices of the Royal Astronomical Society*, 179, 433,  
doi: [10.1093/mnras/179.3.433](https://doi.org/10.1093/mnras/179.3.433)

Bower, G. C., Wright, M. C. H., Falcke, H., & Backer, D. C. 2003, *The Astrophysical Journal*, 588, 331,  
doi: [10.1086/373989](https://doi.org/10.1086/373989)

Carter Edwards, H., Trott, C. R., & Sunderland, D. 2014,  
*Journal of Parallel and Distributed Computing*, 74, 3202,  
doi: <https://doi.org/10.1016/j.jpdc.2014.07.003>

Chael, A., Lupsasca, A., Wong, G. N., & Quataert, E. 2023,  
*ApJ*, 958, 65, doi: [10.3847/1538-4357/acf92d](https://doi.org/10.3847/1538-4357/acf92d)

Chan, H.-S., & Chan, C.-k. 2024, arXiv e-prints,  
arXiv:2408.04132, doi: [10.48550/arXiv.2408.04132](https://doi.org/10.48550/arXiv.2408.04132)

Chan, H.-S., Chan, C.-k., Prather, B. S., Wong, G. N., & Gammie, C. 2024, *ApJ*, 964, 17,  
doi: [10.3847/1538-4357/ad2454](https://doi.org/10.3847/1538-4357/ad2454)

Chandra, M., Gammie, C. F., Foucart, F., & Quataert, E. 2015, *ApJ*, 810, 162, doi: [10.1088/0004-637X/810/2/162](https://doi.org/10.1088/0004-637X/810/2/162)

Chatterjee, K., & Narayan, R. 2022, *The Astrophysical Journal*, 941, 30, doi: [10.3847/1538-4357/ac9d97](https://doi.org/10.3847/1538-4357/ac9d97)

Chatterjee, K., Younsi, Z., Liska, M., et al. 2020, *MNRAS*, 499, 362, doi: [10.1093/mnras/staa2718](https://doi.org/10.1093/mnras/staa2718)

Choi, E., & Wiita, P. J. 2010, *The Astrophysical Journal Supplement Series*, 191, 113,  
doi: [10.1088/0067-0049/191/1/113](https://doi.org/10.1088/0067-0049/191/1/113)

Conroy, N. S., Bauböck, M., Dhruv, V., et al. 2023, *ApJ*, 951, 46, doi: [10.3847/1538-4357/acd2c8](https://doi.org/10.3847/1538-4357/acd2c8)

Davelaar, J., Ripperda, B., Sironi, L., et al. 2023, *ApJL*, 959, L3, doi: [10.3847/2041-8213/ad0b79](https://doi.org/10.3847/2041-8213/ad0b79)

Davis, S. W., & Tchekhovskoy, A. 2020, *ARA&A*, 58, 407,  
doi: [10.1146/annurev-astro-081817-051905](https://doi.org/10.1146/annurev-astro-081817-051905)

De Villiers, J.-P., & Hawley, J. F. 2003, *ApJ*, 589, 458,  
doi: [10.1086/373949](https://doi.org/10.1086/373949)

Del Zanna, L., Zanotti, O., Bucciantini, N., & Londrillo, P. 2007, *A&A*, 473, 11, doi: [10.1051/0004-6361:20077093](https://doi.org/10.1051/0004-6361:20077093)

Dexter, J., Jiménez-Rosales, A., Ressler, S. M., et al. 2020,  
*Monthly Notices of the Royal Astronomical Society*, 494, 4168, doi: [10.1093/mnras/staa922](https://doi.org/10.1093/mnras/staa922)

Dibi, S., Drappeau, S., Fragile, P. C., Markoff, S., & Dexter, J. 2012, *MNRAS*, 426, 1928,  
doi: [10.1111/j.1365-2966.2012.21857.x](https://doi.org/10.1111/j.1365-2966.2012.21857.x)

Doelman, S., Agol, E., Backer, D., et al. 2009, in *astro2010: The Astronomy and Astrophysics Decadal Survey*, Vol. 2010, 68, doi: [10.48550/arXiv.0906.3899](https://doi.org/10.48550/arXiv.0906.3899)

- Eardley, D. M., Lightman, A. P., & Shapiro, S. L. 1975, *ApJL*, 199, L153, doi: [10.1086/181871](https://doi.org/10.1086/181871)
- El Mellah, I., Cerutti, B., & Crinquand, B. 2023, *A&A*, 677, A67, doi: [10.1051/0004-6361/202346781](https://doi.org/10.1051/0004-6361/202346781)
- Event Horizon Telescope Collaboration, Akiyama, K., Alberdi, A., et al. 2019a, *ApJL*, 875, L1, (M87\* Paper I), doi: [10.3847/2041-8213/ab0ec7](https://doi.org/10.3847/2041-8213/ab0ec7)
- . 2019b, *ApJL*, 875, L2, (M87\* Paper II), doi: [10.3847/2041-8213/ab0c96](https://doi.org/10.3847/2041-8213/ab0c96)
- . 2019c, *ApJL*, 875, L3, (M87\* Paper III), doi: [10.3847/2041-8213/ab0c57](https://doi.org/10.3847/2041-8213/ab0c57)
- . 2019d, *ApJL*, 875, L4, (M87\* Paper IV), doi: [10.3847/2041-8213/ab0e85](https://doi.org/10.3847/2041-8213/ab0e85)
- . 2019e, *ApJL*, 875, L5, (M87\* Paper V), doi: [10.3847/2041-8213/ab0f43](https://doi.org/10.3847/2041-8213/ab0f43)
- . 2019f, *ApJL*, 875, L6, (M87\* Paper VI), doi: [10.3847/2041-8213/ab1141](https://doi.org/10.3847/2041-8213/ab1141)
- Event Horizon Telescope Collaboration, Akiyama, K., Algaba, J. C., et al. 2021a, *ApJL*, 910, L12, doi: [10.3847/2041-8213/abe71d](https://doi.org/10.3847/2041-8213/abe71d)
- . 2021b, *ApJL*, 910, L13, doi: [10.3847/2041-8213/abe4de](https://doi.org/10.3847/2041-8213/abe4de)
- Event Horizon Telescope Collaboration, Akiyama, K., Alberdi, A., et al. 2022a, *ApJL*, 930, L12, doi: [10.3847/2041-8213/ac6674](https://doi.org/10.3847/2041-8213/ac6674)
- . 2022b, *ApJL*, 930, L13, doi: [10.3847/2041-8213/ac6675](https://doi.org/10.3847/2041-8213/ac6675)
- . 2022c, *ApJL*, 930, L14, doi: [10.3847/2041-8213/ac6429](https://doi.org/10.3847/2041-8213/ac6429)
- . 2022d, *ApJL*, 930, L15, doi: [10.3847/2041-8213/ac6736](https://doi.org/10.3847/2041-8213/ac6736)
- . 2022e, *ApJL*, 930, L16, doi: [10.3847/2041-8213/ac6672](https://doi.org/10.3847/2041-8213/ac6672)
- . 2022f, *ApJL*, 930, L17, doi: [10.3847/2041-8213/ac6756](https://doi.org/10.3847/2041-8213/ac6756)
- . 2023, *ApJL*, 957, L20, doi: [10.3847/2041-8213/acff70](https://doi.org/10.3847/2041-8213/acff70)
- . 2024, *ApJL*, 964, L25, doi: [10.3847/2041-8213/ad2df0](https://doi.org/10.3847/2041-8213/ad2df0)
- Fishbone, L. G., & Moncrief, V. 1976, *The Astrophysical Journal*, 207, 962, doi: [10.1086/154565](https://doi.org/10.1086/154565)
- Foucart, F., Chandra, M., Gammie, C. F., Quataert, E., & Tchekhovskoy, A. 2017, *Monthly Notices of the Royal Astronomical Society*, 470, 2240, doi: [10.1093/mnras/stx1368](https://doi.org/10.1093/mnras/stx1368)
- Frank, J., King, A. R., & Raine, D. J. 1985, *Accretion power in astrophysics*
- Galishnikova, A., Philippov, A., Quataert, E., et al. 2023, *PhRvL*, 130, 115201, doi: [10.1103/PhysRevLett.130.115201](https://doi.org/10.1103/PhysRevLett.130.115201)
- Gammie, C. F., McKinney, J. C., & Toth, G. 2003, *ApJ*, 589, 444, doi: [10.1086/374594](https://doi.org/10.1086/374594)
- Gammie, C. F., & Popham, R. 1998, *ApJ*, 498, 313, doi: [10.1086/305521](https://doi.org/10.1086/305521)
- Gammie, C. F., Shapiro, S. L., & McKinney, J. C. 2004, *ApJ*, 602, 312, doi: [10.1086/380996](https://doi.org/10.1086/380996)
- Georgiev, B., Pesce, D. W., Broderick, A. E., et al. 2022, *ApJL*, 930, L20, doi: [10.3847/2041-8213/ac65eb](https://doi.org/10.3847/2041-8213/ac65eb)
- Grete, P., Dolence, J. C., Miller, J. M., et al. 2022, *arXiv e-prints*, arXiv:2202.12309, doi: [10.48550/arXiv.2202.12309](https://doi.org/10.48550/arXiv.2202.12309)
- Hawley, J. F., Guan, X., & Krolik, J. H. 2011, *ApJ*, 738, 84, doi: [10.1088/0004-637X/738/1/84](https://doi.org/10.1088/0004-637X/738/1/84)
- Hawley, J. F., Richers, S. A., Guan, X., & Krolik, J. H. 2013, *ApJ*, 772, 102, doi: [10.1088/0004-637X/772/2/102](https://doi.org/10.1088/0004-637X/772/2/102)
- Hopkins, P. F., Grudic, M. Y., Su, K.-Y., et al. 2024, *The Open Journal of Astrophysics*, 7, 18, doi: [10.21105/astro.2309.13115](https://doi.org/10.21105/astro.2309.13115)
- Hou, T. Y., & Lefloch, P. G. 1994, *Mathematics of Computation*, 62, 497
- Howes, G. G. 2010, *Monthly Notices of the Royal Astronomical Society: Letters*, 409, L104, doi: [10.1111/j.1745-3933.2010.00958.x](https://doi.org/10.1111/j.1745-3933.2010.00958.x)
- Ichimaru, S. 1977, *ApJ*, 214, 16
- Igumenshchev, I. V., Narayan, R., & Abramowicz, M. A. 2003, *The Astrophysical Journal*, 592, 1042, doi: [10.1086/375769](https://doi.org/10.1086/375769)
- Inchingolo, G., Grismayer, T., Loureiro, N. F., Fonseca, R. A., & Silva, L. O. 2018, *ApJ*, 859, 149, doi: [10.3847/1538-4357/aac0f2](https://doi.org/10.3847/1538-4357/aac0f2)
- Jacquemin-Ide, J., Lesur, G., & Ferreira, J. 2021, *Astron. Astrophys.*, 647, A192, doi: [10.1051/0004-6361/202039322](https://doi.org/10.1051/0004-6361/202039322)
- Jacquemin-Ide, J., Rincon, F., Tchekhovskoy, A., & Liska, M. 2024, *Mon. Not. R. Astron. Soc.*, 532, 1522, doi: [10.1093/mnras/stae1538](https://doi.org/10.1093/mnras/stae1538)
- Jiang, G.-S., & Shu, C.-W. 1996, *Journal of Computational Physics*, 126, 202, doi: <https://doi.org/10.1006/jcph.1996.0130>
- Joshi, A. V., Prather, B. S., Chan, C.-k., Wielgus, M., & Gammie, C. F. 2024, *ApJ*, 972, 135, doi: [10.3847/1538-4357/ad5b51](https://doi.org/10.3847/1538-4357/ad5b51)
- Kastaun, W., Kalinani, J. V., & Ciolfi, R. 2021, *Phys. Rev. D*, 103, 023018, doi: [10.1103/PhysRevD.103.023018](https://doi.org/10.1103/PhysRevD.103.023018)
- Kawazura, Y., Barnes, M., & Schekochihin, A. A. 2019, *Proc Natl Acad Sci USA*, 116, 771, doi: [10.1073/pnas.1812491116](https://doi.org/10.1073/pnas.1812491116)
- Kim, J.-S., Mueller, H., Nikonov, A. S., et al. 2024, *arXiv e-prints*, arXiv:2409.00540, doi: [10.48550/arXiv.2409.00540](https://doi.org/10.48550/arXiv.2409.00540)
- Kim, J. Y., Krichbaum, T. P., Lu, R. S., et al. 2018, *A&A*, 616, A188, doi: [10.1051/0004-6361/201832921](https://doi.org/10.1051/0004-6361/201832921)
- King, A. 2003, *ApJL*, 596, L27, doi: [10.1086/379143](https://doi.org/10.1086/379143)
- Komissarov, S., & Porth, O. 2021, *NewAR*, 92, 101610, doi: [10.1016/j.newar.2021.101610](https://doi.org/10.1016/j.newar.2021.101610)
- Komissarov, S. S. 1999, *Monthly Notices of the Royal Astronomical Society*, 303, 343, doi: [10.1046/j.1365-8711.1999.02244.x](https://doi.org/10.1046/j.1365-8711.1999.02244.x)

- Kormendy, J., & Richstone, D. 1995, *ARA&A*, 33, 581, doi: [10.1146/annurev.aa.33.090195.003053](https://doi.org/10.1146/annurev.aa.33.090195.003053)
- Kunz, M. W., Schekochihin, A. A., & Stone, J. M. 2014, *Physical Review Letters*, 112, doi: [10.1103/physrevlett.112.205003](https://doi.org/10.1103/physrevlett.112.205003)
- Kunz, M. W., Stone, J. M., & Quataert, E. 2016, *Phys. Rev. Lett.*, 117, 235101, doi: [10.1103/PhysRevLett.117.235101](https://doi.org/10.1103/PhysRevLett.117.235101)
- Lax, P., & Wendroff, B. 1960, *Commun. Pure Appl. Math.*, 13, 217, doi: [10.1002/cpa.3160130205](https://doi.org/10.1002/cpa.3160130205)
- Leung, P. K., Gammie, C. F., & Noble, S. C. 2011, *Astrophys. J.*, 737, 21, doi: [10.1088/0004-637X/737/1/21](https://doi.org/10.1088/0004-637X/737/1/21)
- Lichnerowicz, A. 1967, *Relativistic Hydrodynamics and Magnetohydrodynamics*
- Liska, M., Hesp, C., Tchekhovskoy, A., et al. 2018, *MNRAS*, 474, L81, doi: [10.1093/mnrasl/slx174](https://doi.org/10.1093/mnrasl/slx174)
- Liska, M. T. P., Chatterjee, K., Issa, D., et al. 2022, *ApJS*, 263, 26, doi: [10.3847/1538-4365/ac9966](https://doi.org/10.3847/1538-4365/ac9966)
- Lowell, B., Jacquemin-Ide, J., Tchekhovskoy, A., & Duncan, A. 2024, *ApJ*, 960, 82, doi: [10.3847/1538-4357/ad09af](https://doi.org/10.3847/1538-4357/ad09af)
- Lu, R.-S., Asada, K., Krichbaum, T. P., et al. 2023, *Nature*, 616, 686, doi: [10.1038/s41586-023-05843-w](https://doi.org/10.1038/s41586-023-05843-w)
- Lynden-Bell, D. 1969, *Nature*, 223, 690, doi: [10.1038/223690a0](https://doi.org/10.1038/223690a0)
- Lynden-Bell, D., & Pringle, J. E. 1974, *MNRAS*, 168, 603, doi: [10.1093/mnras/168.3.603](https://doi.org/10.1093/mnras/168.3.603)
- Magorrian, J., Tremaine, S., Richstone, D., et al. 1998, *AJ*, 115, 2285, doi: [10.1086/300353](https://doi.org/10.1086/300353)
- Mahadevan, R., & Quataert, E. 1997, *ApJ*, 490, 605, doi: [10.1086/304908](https://doi.org/10.1086/304908)
- Manikantan, V., Kaaz, N., Jacquemin-Ide, J., et al. 2023, *arXiv e-prints*, arXiv:2310.11490, doi: [10.48550/arXiv.2310.11490](https://doi.org/10.48550/arXiv.2310.11490)
- McKinney, J. C. 2005, *ApJL*, 630, L5, doi: [10.1086/468184](https://doi.org/10.1086/468184)
- McKinney, J. C. 2006, *Monthly Notices of the Royal Astronomical Society*, 368, 1561, doi: [10.1111/j.1365-2966.2006.10256.x](https://doi.org/10.1111/j.1365-2966.2006.10256.x)
- McKinney, J. C., & Gammie, C. F. 2004, *ApJ*, 611, 977, doi: [10.1086/422244](https://doi.org/10.1086/422244)
- McKinney, J. C., Tchekhovskoy, A., & Blandford, R. D. 2012, *Monthly Notices of the Royal Astronomical Society*, 423, 3083, doi: [10.1111/j.1365-2966.2012.21074.x](https://doi.org/10.1111/j.1365-2966.2012.21074.x)
- Mignone, A., & McKinney, J. C. 2007, *Monthly Notices of the Royal Astronomical Society*, 378, 1118, doi: [10.1111/j.1365-2966.2007.11849.x](https://doi.org/10.1111/j.1365-2966.2007.11849.x)
- Mignone, A., Plewa, T., & Bodo, G. 2005, *The Astrophysical Journal Supplement Series*, 160, 199, doi: [10.1086/430905](https://doi.org/10.1086/430905)
- Mishra, B., Begelman, M. C., Armitage, P. J., & Simon, J. B. 2020, *Mon. Not. R. Astron. Soc.*, 492, 1855, doi: [10.1093/mnras/stz3572](https://doi.org/10.1093/mnras/stz3572)
- Mizuno, Y. 2013, *The Astrophysical Journal Supplement Series*, 205, 7, doi: [10.1088/0067-0049/205/1/7](https://doi.org/10.1088/0067-0049/205/1/7)
- Mościbrodzka, M., Falcke, H., Shiokawa, H., & Gammie, C. F. 2014, *A&A*, 570, A7, doi: [10.1051/0004-6361/201424358](https://doi.org/10.1051/0004-6361/201424358)
- Mościbrodzka, M., Falcke, H., & Shiokawa, H. 2016, *A&A*, 586, A38, doi: [10.1051/0004-6361/201526630](https://doi.org/10.1051/0004-6361/201526630)
- Narayan, R., Chael, A., Chatterjee, K., Ricarte, A., & Curd, B. 2022, *MNRAS*, 511, 3795, doi: [10.1093/mnras/stac285](https://doi.org/10.1093/mnras/stac285)
- Narayan, R., Igumenshchev, I. V., & Abramowicz, M. A. 2003, *Publications of the Astronomical Society of Japan*, 55, L69, doi: [10.1093/pasj/55.6.L69](https://doi.org/10.1093/pasj/55.6.L69)
- Narayan, R., Sądowski, A., Penna, R. F., & Kulkarni, A. K. 2012, *Monthly Notices of the Royal Astronomical Society*, 426, 3241, doi: [10.1111/j.1365-2966.2012.22002.x](https://doi.org/10.1111/j.1365-2966.2012.22002.x)
- Narayan, R., & Yi, I. 1994, *ApJL*, 428, L13, doi: [10.1086/187381](https://doi.org/10.1086/187381)
- . 1995, *ApJ*, 444, 231, doi: [10.1086/175599](https://doi.org/10.1086/175599)
- Narayan, R., Yi, I., & Mahadevan, R. 1995, *Nature*, 374, 623, doi: [10.1038/374623a0](https://doi.org/10.1038/374623a0)
- Nathanail, A., Fromm, C. M., Porth, O., et al. 2020, *MNRAS*, 495, 1549, doi: [10.1093/mnras/staa1165](https://doi.org/10.1093/mnras/staa1165)
- Noble, S. C., Gammie, C. F., McKinney, J. C., & Del Zanna, L. 2006, *ApJ*, 641, 626, doi: [10.1086/500349](https://doi.org/10.1086/500349)
- Noble, S. C., Krolik, J. H., & Hawley, J. F. 2010, *ApJ*, 711, 959, doi: [10.1088/0004-637X/711/2/959](https://doi.org/10.1088/0004-637X/711/2/959)
- Novikov, I. D., & Thorne, K. S. 1973, in *Black Holes (Les Astres Occlus)*, 343–450
- Page, D. N., & Thorne, K. S. 1974, *ApJ*, 191, 499, doi: [10.1086/152990](https://doi.org/10.1086/152990)
- Papaloizou, J. C. B., & Lin, D. N. C. 1995, *ARA&A*, 33, 505, doi: [10.1146/annurev.aa.33.090195.002445](https://doi.org/10.1146/annurev.aa.33.090195.002445)
- Penna, R. F., Kulkarni, A., & Narayan, R. 2013, *A&A*, 559, A116, doi: [10.1051/0004-6361/201219666](https://doi.org/10.1051/0004-6361/201219666)
- Penna, R. F., McKinney, J. C., Narayan, R., et al. 2010, *MNRAS*, 408, 752, doi: [10.1111/j.1365-2966.2010.17170.x](https://doi.org/10.1111/j.1365-2966.2010.17170.x)
- Popham, R., & Gammie, C. F. 1998, *ApJ*, 504, 419, doi: [10.1086/306054](https://doi.org/10.1086/306054)
- Porth, O., Olivares, H., Mizuno, Y., et al. 2017, *Computational Astrophysics and Cosmology*, 4, 1, doi: [10.1186/s40668-017-0020-2](https://doi.org/10.1186/s40668-017-0020-2)
- Porth, O., Chatterjee, K., Narayan, R., et al. 2019, *The Astrophysical Journal Supplement Series*, 243, 26, doi: [10.3847/1538-4365/ab29fd](https://doi.org/10.3847/1538-4365/ab29fd)
- Prather, B. 2022, *Ph.D. Thesis*
- Prather, B. S. 2024, *arXiv*, doi: [10.48550/arXiv.2408.01361](https://doi.org/10.48550/arXiv.2408.01361)

- Prather, B. S., Wong, G. N., Dhruv, V., et al. 2021, *Journal of Open Source Software*, 6, 3336, doi: [10.21105/joss.03336](https://doi.org/10.21105/joss.03336)
- Pringle, J. E. 1981, *ARA&A*, 19, 137, doi: [10.1146/annurev.aa.19.090181.001033](https://doi.org/10.1146/annurev.aa.19.090181.001033)
- Quataert, E., & Gruzinov, A. 2000, *ApJ*, 545, 842, doi: [10.1086/317845](https://doi.org/10.1086/317845)
- Rees, M. J., Begelman, M. C., Blandford, R. D., & Phinney, E. S. 1982, *Nature*, 295, 17, doi: [10.1038/295017a0](https://doi.org/10.1038/295017a0)
- Ressler, S. M., Tchekhovskoy, A., Quataert, E., Chandra, M., & Gammie, C. F. 2015, *Mon. Not. R. Astron. Soc.*, 454, 1848, doi: [10.1093/mnras/stv2084](https://doi.org/10.1093/mnras/stv2084)
- Ressler, S. M., Tchekhovskoy, A., Quataert, E., & Gammie, C. F. 2017, *MNRAS*, 467, 3604, doi: [10.1093/mnras/stx364](https://doi.org/10.1093/mnras/stx364)
- Ressler, S. M., White, C. J., & Quataert, E. 2023, *MNRAS*, 521, 4277, doi: [10.1093/mnras/stad837](https://doi.org/10.1093/mnras/stad837)
- Ressler, S. M., White, C. J., Quataert, E., & Stone, J. M. 2020, *ApJL*, 896, L6, doi: [10.3847/2041-8213/ab9532](https://doi.org/10.3847/2041-8213/ab9532)
- Richstone, D., Ajhar, E. A., Bender, R., et al. 1998, *Nature*, 385, A14, doi: [10.48550/arXiv.astro-ph/9810378](https://doi.org/10.48550/arXiv.astro-ph/9810378)
- Ripperda, B., Bacchini, F., & Philippov, A. A. 2020, *ApJ*, 900, 100, doi: [10.3847/1538-4357/ababab](https://doi.org/10.3847/1538-4357/ababab)
- Ripperda, B., Liska, M., Chatterjee, K., et al. 2022, *ApJL*, 924, L32, doi: [10.3847/2041-8213/ac46a1](https://doi.org/10.3847/2041-8213/ac46a1)
- Riquelme, M., Quataert, E., & Verscharen, D. 2018, *The Astrophysical Journal*, 854, 132, doi: [10.3847/1538-4357/aaa6d1](https://doi.org/10.3847/1538-4357/aaa6d1)
- Riquelme, M. A., Quataert, E., & Verscharen, D. 2016, *The Astrophysical Journal*, 824, 123, doi: [10.3847/0004-637x/824/2/123](https://doi.org/10.3847/0004-637x/824/2/123)
- Rowan, M. E., Sironi, L., & Narayan, R. 2017, *ApJ*, 850, 29, doi: [10.3847/1538-4357/aa9380](https://doi.org/10.3847/1538-4357/aa9380)
- Rusanov, V. 1962, *USSR Computational Mathematics and Mathematical Physics*, 1, 304, doi: [https://doi.org/10.1016/0041-5553\(62\)90062-9](https://doi.org/10.1016/0041-5553(62)90062-9)
- Ryan, B. R., Ressler, S. M., Dolence, J. C., Gammie, C., & Quataert, E. 2018, *The Astrophysical Journal*, 864, 126, doi: [10.3847/1538-4357/aad73a](https://doi.org/10.3847/1538-4357/aad73a)
- Ryan, B. R., Ressler, S. M., Dolence, J. C., et al. 2017, *The Astrophysical Journal*, 844, L24, doi: [10.3847/2041-8213/aa8034](https://doi.org/10.3847/2041-8213/aa8034)
- Salas, L. D. S., Musoke, G., Chatterjee, K., et al. 2024, *MNRAS*, 533, 254, doi: [10.1093/mnras/stae1834](https://doi.org/10.1093/mnras/stae1834)
- Sano, T., Inutsuka, S., Turner, N. J., & Stone, J. M. 2004, *ApJ*, 605, 321, doi: [10.1086/382184](https://doi.org/10.1086/382184)
- Scepi, N., Begelman, M. C., & Dexter, J. 2023, *Monthly Notices of the Royal Astronomical Society*, 527, 1424, doi: [10.1093/mnras/stad3299](https://doi.org/10.1093/mnras/stad3299)
- Scepi, N., Dexter, J., & Begelman, M. C. 2022, *MNRAS*, 511, 3536, doi: [10.1093/mnras/stac337](https://doi.org/10.1093/mnras/stac337)
- Shakura, N. I., & Sunyaev, R. A. 1973, *A&A*, 24, 337
- Shapiro, S. L. 2005, *ApJ*, 620, 59, doi: [10.1086/427065](https://doi.org/10.1086/427065)
- Shapiro, S. L., Lightman, A. P., & Eardley, D. M. 1976, *ApJ*, 204, 187, doi: [10.1086/154162](https://doi.org/10.1086/154162)
- Shiokawa, H., Dolence, J. C., Gammie, C. F., & Noble, S. C. 2012, *ApJ*, 744, 187, doi: [10.1088/0004-637X/744/2/187](https://doi.org/10.1088/0004-637X/744/2/187)
- Silk, J., & Rees, M. J. 1998, *A&A*, 331, L1, doi: [10.48550/arXiv.astro-ph/9801013](https://doi.org/10.48550/arXiv.astro-ph/9801013)
- Sironi, L. 2015, *ApJ*, 800, 89, doi: [10.1088/0004-637X/800/2/89](https://doi.org/10.1088/0004-637X/800/2/89)
- Sironi, L., & Narayan, R. 2015, *The Astrophysical Journal*, 800, 88, doi: [10.1088/0004-637x/800/2/88](https://doi.org/10.1088/0004-637x/800/2/88)
- Sądowski, A., Narayan, R., Tchekhovskoy, A., & Zhu, Y. 2013, *MNRAS*, 429, 3533, doi: [10.1093/mnras/sts632](https://doi.org/10.1093/mnras/sts632)
- Sądowski, A., Wielgus, M., Narayan, R., et al. 2017, *MNRAS*, 466, 705, doi: [10.1093/mnras/stw3116](https://doi.org/10.1093/mnras/stw3116)
- Stone, J. M., & Gardiner, T. 2009, *NewA*, 14, 139, doi: [10.1016/j.newast.2008.06.003](https://doi.org/10.1016/j.newast.2008.06.003)
- Sądowski, A., Narayan, R., Penna, R., & Zhu, Y. 2013, *Monthly Notices of the Royal Astronomical Society*, 436, 3856, doi: [10.1093/mnras/stt1881](https://doi.org/10.1093/mnras/stt1881)
- Tchekhovskoy, A., & McKinney, J. C. 2012, *Monthly Notices of the Royal Astronomical Society: Letters*, 423, L55, doi: [10.1111/j.1745-3933.2012.01256.x](https://doi.org/10.1111/j.1745-3933.2012.01256.x)
- Tchekhovskoy, A., McKinney, J. C., & Narayan, R. 2012, *J. Phys.: Conf. Ser.*, 372, 012040, doi: [10.1088/1742-6596/372/1/012040](https://doi.org/10.1088/1742-6596/372/1/012040)
- Tchekhovskoy, A., Narayan, R., & McKinney, J. C. 2010, *ApJ*, 711, 50, doi: [10.1088/0004-637X/711/1/50](https://doi.org/10.1088/0004-637X/711/1/50)
- Tchekhovskoy, A., Narayan, R., & McKinney, J. C. 2011, *Monthly Notices of the Royal Astronomical Society: Letters*, 418, L79, doi: [10.1111/j.1745-3933.2011.01147.x](https://doi.org/10.1111/j.1745-3933.2011.01147.x)
- The Event Horizon Telescope Collaboration, Akiyama, K., Alberdi, A., et al. 2024, *Astrophys. J. Lett.*, 964, L26, doi: [10.3847/2041-8213/ad2df1](https://doi.org/10.3847/2041-8213/ad2df1)
- Thorne, K. S. 1974, *ApJ*, 191, 507, doi: [10.1086/152991](https://doi.org/10.1086/152991)
- Tóth, G. 2000, *Journal of Computational Physics*, 161, 605
- Trott, C., Berger-Vergiat, L., Poliakov, D., et al. 2021, *Computing in Science & Engineering*, 23, 10, doi: [10.1109/MCSE.2021.3098509](https://doi.org/10.1109/MCSE.2021.3098509)
- Trott, C. R., Lebrun-Grandié, D., Arndt, D., et al. 2022, *IEEE Transactions on Parallel and Distributed Systems*, 33, 805, doi: [10.1109/TPDS.2021.3097283](https://doi.org/10.1109/TPDS.2021.3097283)
- Vos, J. T., Olivares, H., Cerutti, B., & Mościbrodzka, M. 2024, *MNRAS*, 531, 1554, doi: [10.1093/mnras/stae1046](https://doi.org/10.1093/mnras/stae1046)
- Walker, R. C., Hardee, P. E., Davies, F. B., Ly, C., & Junor, W. 2018, *ApJ*, 855, 128, doi: [10.3847/1538-4357/aaafcc](https://doi.org/10.3847/1538-4357/aaafcc)

- Werner, G. R., Uzdensky, D. A., Begelman, M. C., Cerutti, B., & Nalewajko, K. 2018, *Monthly Notices of the Royal Astronomical Society*, 473, 4840, doi: [10.1093/mnras/stx2530](https://doi.org/10.1093/mnras/stx2530)
- White, C. J., Quataert, E., & Gammie, C. F. 2020, *ApJ*, 891, 63, doi: [10.3847/1538-4357/ab718e](https://doi.org/10.3847/1538-4357/ab718e)
- White, C. J., Stone, J. M., & Quataert, E. 2019, *ApJ*, 874, 168, doi: [10.3847/1538-4357/ab0c0c](https://doi.org/10.3847/1538-4357/ab0c0c)
- Wielgus, M., Marchili, N., Martí-Vidal, I., et al. 2022, *Astrophys. J. Lett.*, 930, L19, doi: [10.3847/2041-8213/ac6428](https://doi.org/10.3847/2041-8213/ac6428)
- Wilson, L. A. 2017, *Big Data Research*, 8, 57, doi: <https://doi.org/10.1016/j.bdr.2017.04.001>
- Wong, G. N., Du, Y., Prather, B. S., & Gammie, C. F. 2021, *The Astrophysical Journal*, 914, 55, doi: [10.3847/1538-4357/abf8b8](https://doi.org/10.3847/1538-4357/abf8b8)
- Wong, G. N., Prather, B. S., Dhruv, V., et al. 2022, *The Astrophysical Journal Supplement Series*, 259, 64, doi: [10.3847/1538-4365/ac582e](https://doi.org/10.3847/1538-4365/ac582e)
- Yuan, F., Gan, Z., Narayan, R., et al. 2015, *ApJ*, 804, 101, doi: [10.1088/0004-637X/804/2/101](https://doi.org/10.1088/0004-637X/804/2/101)
- Zhdankin, V., Uzdensky, D. A., & Kunz, M. W. 2021, *ApJ*, 908, 71, doi: [10.3847/1538-4357/abcf31](https://doi.org/10.3847/1538-4357/abcf31)